Drag Measurements on an Ellipsoidal Body

Joshua Andrew DeMoss

Thesis submitted to the faculty of the Virginia Polytechnic Institute and State University in partial fulfillment of the requirements for the degree of

Master of Science
In
Aerospace Engineering

Dr. Roger L. Simpson (Chair)
Dr. William J. Devenport
Dr. Wayne L. Neu

August 21, 2007
Blacksburg, Virginia

Keywords: Multi-hole probe, Seven-hole probe, Ellipsoid, Non-body of Revolution, Drag Measurement, Wake Measurement, Subsonic Aerodynamics

Drag Measurements on an Ellipsoidal Body

Joshua Andrew DeMoss

Abstract

A drag study was conducted on an oblate ellipsoid body in the Virginia Tech Stability Wind Tunnel. Two-dimensional wake surveys were taken with a seven-hole probe and an integral momentum method was applied to the results to calculate the drag on the body. Several different model configurations were tested; these included the model oriented at a 0° and 10° angle of attack with respect to the oncoming flow. For both angles, the model was tested with and without flow trip strips. At the 0° angle of attack orientation, data were taken at a speed of 44 m/s. Data with the model at a 10° angle of attack were taken at 44 m/s and 16 m/s. The high speed flow corresponded to a length-based Reynolds number of about 4.3 million; the low speed flow gave a Reynolds number of about 1.6 million. The results indicated that the length-squared drag coefficients ranged from around 0.0026 for the 0° angle of attack test cases and 0.0035 for the 10° angle of attack test cases. The 10° angle of attack cases had higher drag due to the increase in the frontal profile area of the model and the addition of induced drag. The flow trip strips appeared to have a tiny effect on the drag; a slight increase in drag coefficient was seen by their application but it was not outside of the uncertainty in the calculation. At the lower speed, uncertainties in the calculation were so high that the drag results could not be considered with much confidence, but the drag coefficient did decrease from the higher Reynolds number cases. Uncertainty in the drag calculations derived primarily from spatial fluctuations of the mean velocity and total pressure in the wake profile; uncertainty was estimated to be about 16% or less for the 44 m/s test cases.

Acknowledgements

This work was supported by The US Office of Naval Research (ONR) under Grant N00014-06-1-0591 monitored by Program Manager Dr. Ron Joslin and by Northrup-Grumman Newport News Shipbuilding Co. This support is gratefully appreciated.

I would like to thank Kenneth Granlund for his significant contributions to this study. Kenneth built the ellipsoid model used in these tests and greatly assisted in the experimental setup. He then volunteered as a shift leader in the wind tunnel, which allowed for two eight-hour testing shifts to be run per day. This maximized the amount of data that could be taken in the ten-day test period that was allotted. Without his help, this study could not have taken place.

My advisor, Dr. Roger L. Simpson provided tremendous guidance, support, and patience throughout this study. His knowledge and assistance ensured that the tests were properly conducted.

Andrew Hopkins worked especially hard with me in the experimental setup, aided in the seven-hole probe software development, and contributed some time to the testing of the model in the Stability Wind Tunnel. Shereef Sadek was instrumental in helping to develop the seven-hole probe software and data reduction process. Thanks also goes to Bruce Stanger, Steve Edwards, and Bill Oetjens of Virginia Tech's Department for Aerospace and Ocean Engineering for their help in developing and setting up the seven-hole probe hardware in the Stability Wind Tunnel.

Acknowledgements

The following graduate students volunteered a significant amount of their time to serve on the testing shifts in the Stability Wind Tunnel: Qing Tian, Todd Lowe, Deirdre Hunter, and Nathaniel Varano. Their assistance was greatly appreciated.

Finally, I would like to thank my wife and family for their never-ending support and encouragement throughout this study.

Table of Contents

List of Tables

List of Figures

Nomenclature

Roman

A	Wind tunnel cross-sectional area: 3.35 m^2
b_1, b_2, A_t, A_s	Non-dimensional pressure coefficients for low and high incidence angles: (Equations 1 and 2)
c_{0j}, c_{1j}, c_{2j}	Coefficients from the seven-hole probe's interpolation of calibration data: (Equation 3)
C_D	Drag coefficient
C_{DF}	Frontal area drag coefficient: $C_{DF} = \frac{D}{0.5\rho U_\infty^2 FA}$
C_{DL}	Length-squared drag coefficient: $C_{DL} = \frac{D}{0.5\rho U_\infty^2 L^2}$
C_{DW}	Wetted area drag coefficient: $C_{DW} = \frac{D}{0.5\rho U_\infty^2 WA}$
C_L	Lift coefficient
C_{LF}	Frontal area lift coefficient: $C_{LF} = \frac{Lift}{0.5\rho U_\infty^2 FA}$
C_{LL}	Length-squared lift coefficient: $C_{LL} = \frac{Lift}{0.5\rho U_\infty^2 L^2}$
C_{LW}	Wetted area lift coefficient: $C_{LW} = \frac{Lift}{0.5\rho U_\infty^2 WA}$
D	Total drag on the body: $D = D_p + D_i$
D_i	Induced drag on the body: $D_i \approx \frac{\rho}{2} \iint_{Wake} [\Psi\xi - \Phi\sigma] ds$
D_p	Profile drag on the body: $D_p = \iint_{Wake} \left[P_{t\infty} - P_t + \frac{\rho(U^* - U)(U^* + U - 2U_\infty)}{2} \right] ds$
FA	Frontal area of the body: 0.0726 m^2

k	Relaminarization factor: $k = \frac{\nu_e}{U_e^2}\frac{dU_e}{dx}$
L	Length of model: 1.6 m
M	Flow Mach number, from probe: $M = \sqrt{5\left[\left(\frac{P_t}{P}\right)^{2/7} - 1\right]}$
$\vec{n}$	Surface normal vector
P	Static pressure, from probe: $P = P_t - \frac{q}{A_s}$
P_1, P_2, P_3, P_4, P_5, P_6, P_7	Pressures from the seven ports of the seven-hole probe
$P_{i\max}$	Maximum pressure from the seven ports of the seven-hole probe
P^+, P^-	Pressure from the port next to the port reading the maximum pressure in the clockwise and counter-clockwise direction, respectively
P_t	Total pressure, from probe: $P_t = P_{i\max} - qA_t$
$P_{t\infty}$	Free-stream total pressure
q	Pseudo-dynamic pressure: (Equations 1 and 2)
R	Gas constant
$\mathrm{Re_L}$	Length based Reynolds number: $\mathrm{Re}_L = \frac{U_\infty L}{\nu_\infty}$
T	Flow temperature, from probe: $T = \frac{T_t}{\left(1 + M^2/5\right)}$
T_t	Flow total temperature
t	Total data sampling time: $t = \frac{200L}{U_\infty}$
U, V, W	Stream-wise, normal, and span-wise velocity, respectively

u, v, w	Stream-wise, normal, and span-wise perturbation velocity, respectively
$\vec{U}$	Velocity vector
U_b	Uniform blockage velocity: $U_b = \frac{1}{2A}\iint_{Wake}(U^* - U)ds$
U_e	Boundary layer edge velocity
U_n	Normal component of the velocity vector
U_t	Tangential component of the velocity vector
U_∞	Free-stream velocity
U'	Perturbation velocity: $U' = U^* - U_\infty$
U^*	Artificial axial velocity: $U^* = \sqrt{U^2 + \frac{2(P_{t\infty} - P_t)}{\rho}}$
WA	Wetted area on body: 1.487 m^2
x, y, z	Coordinates in the stream-wise, normal, and span-wise direction, respectively

Greek

α	Seven-hole probe pitch angle: $\alpha = \alpha(b_1, b_2) = c_{0\alpha} + c_{1\alpha} b_1 + c_{2\alpha} b_2$
β	Seven-hole probe yaw angle: $\beta = \beta(b_1, b_2) = c_{0\beta} + c_{1\beta} b_1 + c_{2\beta} b_2$
γ	Ratio of specific heats
Γ	Circulation: $\Gamma = \iint_{Wake} [\xi] ds$
ν_e	Boundary layer edge kinematic viscosity
ν_∞	Free-stream kinematic viscosity
ξ	Axial component of the vorticity: $\xi = \frac{\partial W}{\partial y} - \frac{\partial V}{\partial z}$
ρ	Density
σ	Cross-flow divergence: $\sigma = \frac{\partial V}{\partial y} + \frac{\partial W}{\partial z} = \frac{-\partial U}{\partial x}$
Φ	Velocity potential: $\frac{\partial^2 \Phi}{\partial y^2} + \frac{\partial^2 \Phi}{\partial z^2} = \sigma$
Ψ	Stream function: $\frac{\partial^2 \Psi}{\partial y^2} + \frac{\partial^2 \Psi}{\partial z^2} = -\xi$
$\vec{\Omega}$	Vorticity vector

1 Introduction

1.1 Purpose

The main goal of this study was to experimentally measure the drag of an oblate ellipsoid body in the Virginia Tech Stability Wind Tunnel. Since experimental measurements on non-body of revolution models are very scant, this study expands current databases by providing a significant amount of information on a body with an ellipsoidal shape and cross-section. The other objective of this study was to demonstrate the effectiveness of a seven-hole probe in obtaining the drag on the ellipsoid body from data acquired by wake surveys.

To accomplish these objectives, a 1.6 m long model having an elliptic cross-section of 0.4 m x 0.231 m was constructed from composite materials. The model was suspended with guy wires in the Stability Wind Tunnel and 2-D wake surveys were taken using a seven-hole probe. The pressure data from each probe survey were then reduced to determine the velocity profile of the model's wake. The drag was then calculated by applying the integral momentum theorem to the wake velocity profile. Additional information on the circulation and lift on the model was obtained by integrating the stream-wise vorticity that was formed from counter-rotating vortices emanating from the model at a 10° angle of attack.

The experiment was conducted under several different flow conditions and model configurations to determine their effects on the drag measurements. Data were collected with the model in a straight-and-level position (0° angle of attack, yaw, and roll) and a 10° angle of attack position (0° yaw and roll) with respect to the oncoming flow. For

both model positions, data were taken with and without flow trip strips. At the 0° angle of attack position, data were taken at a speed of 44 m/s. At the 10° angle of attack position, tests were conducted at two different speeds (44 m/s and 16 m/s) to show some of the effect of the Reynolds number on the drag. These speeds gave length-based Reynolds numbers of 4.3 and 1.6 million, respectively.

The tests on the ellipsoid body were part of a much larger drag study that took place on the Newport News Experimental Model One (NNEMO) body. Funding for these tests was provided primarily to make measurements on the NNEMO body and secondary priority was given to making measurements on the ellipsoid model. For this reason, after testing on the NNEMO had concluded, there was only time to perform five ellipsoid test cases in the Stability Wind Tunnel. As a result, the drag study on the ellipsoid is not nearly as detailed as it could be. For example, more than two different flow speeds could have been tested at both angles of attack to determine better the effects of Reynolds number on the drag. Two different ways of tripping the flow on the model were also available, but only one could be utilized due to time constraints. Finally, other model configurations at different angles of attack, roll, or yaw could have been tested as well, to provide a better overall picture of the drag on the body.

1.2 Background

1.2.1 Drag Measurement Techniques

There are many ways to calculate the drag of 3-D bodies in a wind tunnel. Perhaps the most common and widely used approach is to mount a model on a sting that

is equipped with a force balance. While this may be the simplest approach, there are several problems with this method including: accounting for the flow distortion and interference drag from the sting and having to make modifications to the model to accommodate the sting.

Due to these problems, other methods have been developed in an effort to minimize or eliminate support interference. One of the most modern techniques is the use of a magnetic suspension and balance system (MSBS). A MSBS uses a system of electromagnets in tandem with laser positioning equipment to hold a model at a certain position in a wind tunnel without the use of any supports. Drag forces on the model are then measured by recording the change in electro-magnetic force that is required to hold the model in position. Obviously, the elimination of a model support system allows MSBS to very accurately calculate the drag and other aerodynamic forces on a model. Figure 1.1 from Dress (1990) shows the difference in the wetted area drag coefficients produced between a sting-mounted prolate spheroid model and a support-free MSBS system. Dress (1990) reports that the sting acts as an extension to the model, creating a higher fineness ratio shape to reduce the drag. The sting also serves to alter or breakup the separated wake at the stern of the model, further reducing the drag.

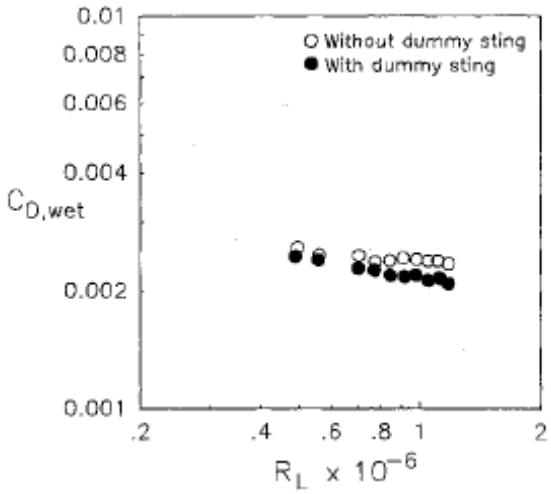

Figure 1.1: Comparison of Prolate Spheroid Drag Coefficients Measured Using a Sting and an MSBS System (Adapted from Dress, 1990)

The problem with a MSBS system, however, is its extreme expense and complexity of use. Since there is no MSBS system available for use at Virginia Tech, a different technique to measure drag was employed for this study. Thus, a guy wire suspension apparatus and a seven-hole probe wake surveying system were employed as a compromise between the MSBS and sting support system. Quite simply, the wire suspension system significantly reduces the size of the model support system and allows the seven-hole probe to survey the wake so that a momentum balance could be used to calculate the drag on the model. See Sections 2 and 3 of this paper for detailed information on the guy wire suspension system and drag measurement technique.

1.2.2 Previous Drag Results for Ellipsoids and Similar Bodies

Drag research on oblate ellipsoids and other non-bodies of revolution is very scant as there are few real world examples of such bodies. However, there is much literature with drag information on bodies of revolution such as prolate ellipsoids and spheroids that can serve as a baseline reference to the work performed in this study. Hoerner (1965) presents the wetted area drag coefficients of numerous shapes including 3-D

bodies of revolution. Figure 1.2 presents wetted area drag coefficients of several of bodies of revolution with different fineness ratios over a range of Reynolds numbers.

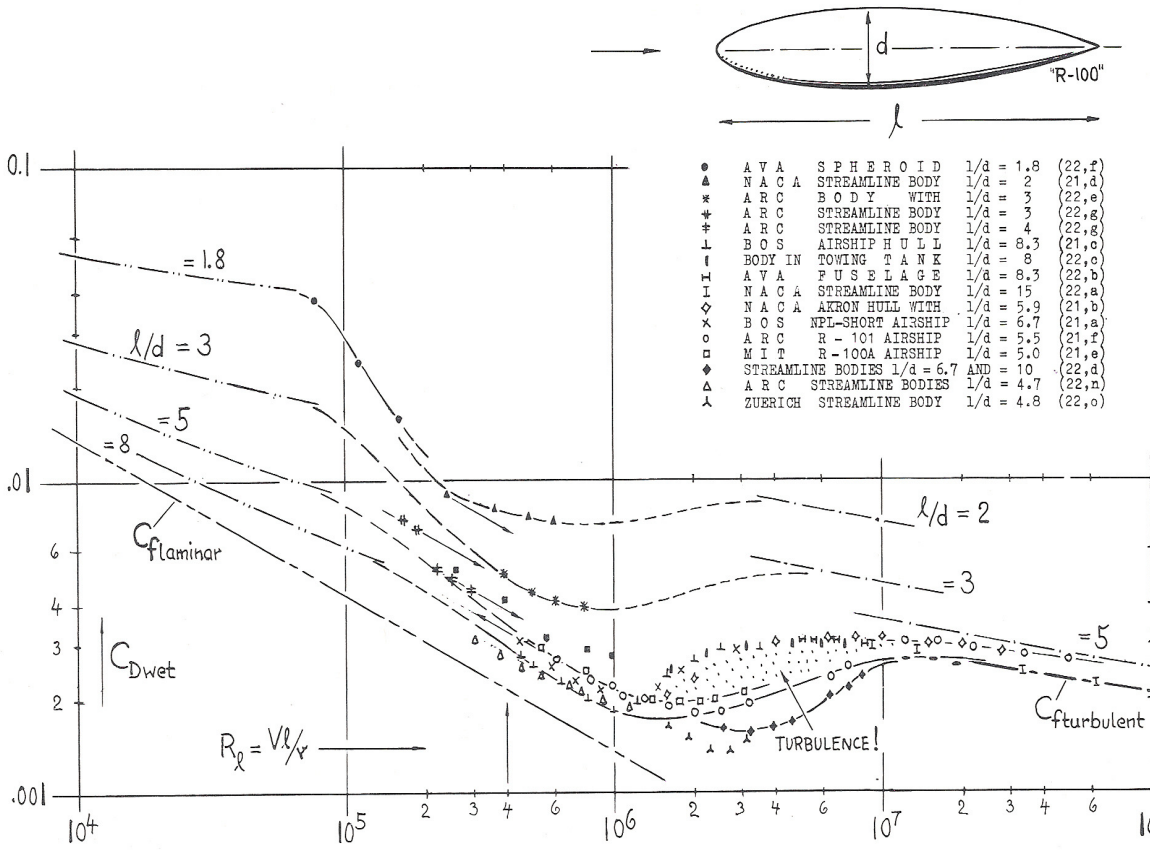

Figure 1.2: Drag Data on 3-D Bodies of Revolution Aligned Straight-and-Level (Adapted from Hoerner, 1965)

From Figure 1.2, the effect of Reynolds number and fineness ratio is evident. At Reynolds numbers below 10^5, the boundary layer flow is completely laminar and drag coefficients tend to be at their highest overall value. Then a critical Reynolds number is reached between 10^5 and 10^6, where the boundary layer flow begins to undergo a transition from laminar to turbulent and a dramatic drop is seen in the drag coefficients. After reaching a minimum, the drag coefficients rise again slightly, as the boundary layer flow moves towards being fully turbulent between Reynolds numbers of 10^6 and 10^7. Finally, after reaching a Reynolds number of around 10^7, the boundary layer flow

becomes fully turbulent and the drag coefficients decrease again. Through all of the Reynolds numbers, the effect of the fineness ratio is the same with higher fineness ratios generally producing lower drag coefficients.

It is difficult to apply the data in Figure 1.2 to predict precisely the results of this drag study on the oblate ellipsoid. However, a range for the drag coefficient on the model may be estimated. Since the oblate ellipsoid is not a body of revolution, it does not have a clearly defined fineness ratio; the length-to-width ratio is 4:1, while the length-to-height ratio is 6.93:1. If compared to a body of revolution with the ellipsoid's width as its diameter and a fineness ratio of 4, the ellipsoid may have a smaller wetted area and drag coefficient. If compared to a body of revolution with the same diameter as the ellipsoid's height and a fineness ratio of 6.93, the ellipsoid may have a larger wetted area and drag coefficient. At a Reynolds number of 4 million, which is close to the straight-and-level test cases' Reynolds number in this study, bodies with a fineness ratio between 5 and 10 in Figure 1.2 are typically seen to have wetted area drag coefficients between 0.002 and 0.003. Figure 1.2 also shows that bodies with a fineness ratio between 3 and 5 have drag coefficients between 0.003 and 0.006. If it is assumed that the ellipsoid will have a wetted area drag coefficient somewhere between a body of revolution of fineness ratio 4 and 6.93, the range of possible drag coefficients probably lies between 0.002 and 0.006 for the model in a straight-and-level configuration.

There were two different Reynolds numbers tested in this study, 1.6 and 4.3 million. Judging from Figure 1.2, one might expect that the model at a Reynolds number of 1.6 million would have a lower drag coefficient than that at 4.3 million. But since it is difficult to pinpoint the critical Reynolds number on the oblate ellipsoid where the

boundary layer flow will transition from laminar to turbulent, making accurate drag coefficient predictions with the two Reynolds numbers may not be possible. For example, Figure 1.3 from Dress (1990) shows the wetted area drag coefficient for a 7.5:1 prolate spheroid from several different tests. Here, the critical Reynolds number is reached around 1 million and the minimum drag coefficient is at 4 million. This is quite different than what was seen in Figure 1.2. So, a prediction on whether the model at a 1.6 million Reynolds number will have a lower drag coefficient than it would at 4.3 million is probably not possible.

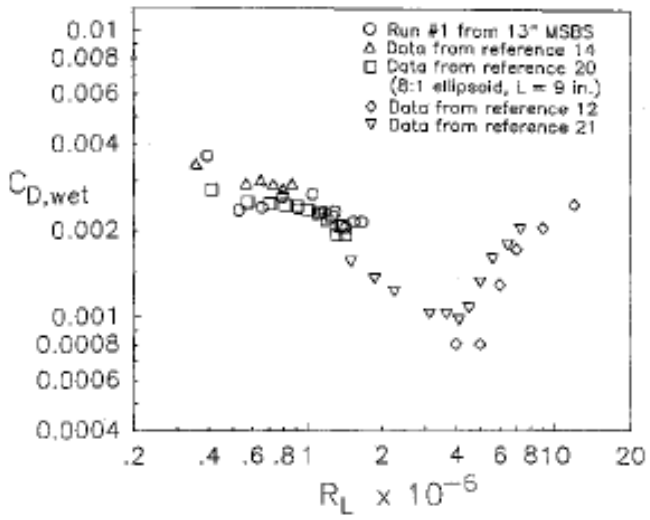

Figure 1.3: Drag Data from a 7.5:1 Prolate Spheroid Aligned Straight-and-Level (Adapted from Dress, 1990)

1.2.3 The NNEMO Drag Study

As mentioned in Section 1.1, a much larger drag study was performed on the NNEMO model immediately prior to the tests on the ellipsoid body (DeMoss and Simpson, 2006). These tests utilized the exact same setup and methods that were used in the ellipsoid study. Additionally, oil flows were performed for flow visualization and to locate separation regions on the model.

The NNEMO is a larger body than the ellipsoid and has a set of forward and aft appendages as well as a large sail; like the ellipsoid, the NNEMO is a non-body of revolution model. Figure 1.4 shows the NNEMO model mounted in the Stability Wind Tunnel.

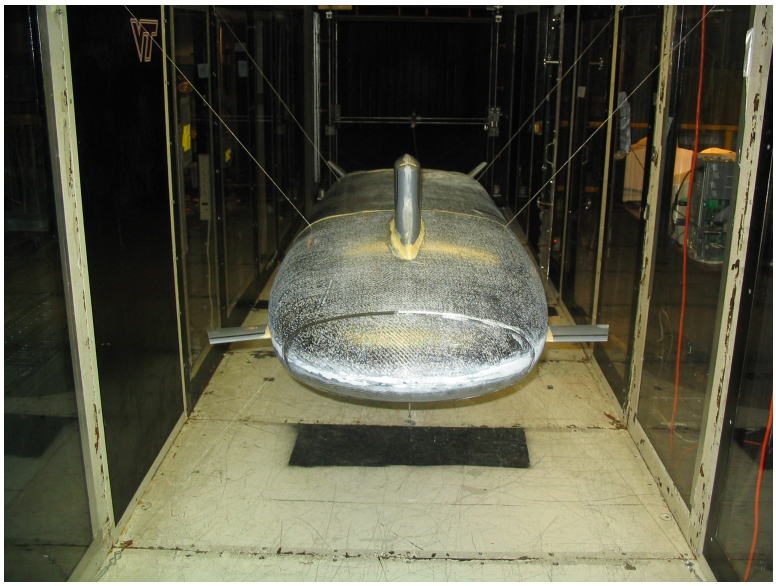

Figure 1.4: NNEMO Model Mounted in the Stability Tunnel

Several different model configurations were tested; these included the bare hull with and without flow trips, the appended model with and without flow trips, and the appended model with the main sail set to a forward and then aft position. Data were taken near Reynolds numbers of 2.7 and 1.0 million per meter with the model in a straight-and-level position.

Some of the more significant results indicated that the appended model with the sail set aft produced the highest drag coefficients of all the configurations. Setting the sail forward on the appended model significantly reduced the drag coefficient. Oil flows were used to investigate this result and indicated that moving the sail forward on the

model significantly decreased the area of flow separation on the stern, thereby decreasing the drag.

It was also found that the low Reynolds number, non-appended model configurations produced higher drag coefficients compared to the high Reynolds number non-appended model configurations. Two methods of flow tripping were utilized on the model and both did not have much of an effect on the drag results; the drag coefficient was seen to increase slightly from the non-tripped cases, but this increase was smaller than the level of uncertainty attributed to the results. Finally, other oil flows on the model, without the sail attached, failed to show anything of significance. Because of this and time constraints it was decided that performing oil flows on the ellipsoid model would not be very worthwhile.

The drag results from the NNEMO tests were sent to the Newport News Shipyard after the data analysis had concluded. Feedback has been very positive, as the drag numbers were reportedly very close to those calculated by CFD simulations that had been run on the model and other drag studies that had been performed. However, these other results from the Shipyard were and are not currently available to be reported in this study. The success of the NNEMO study is very encouraging and helps to validate the methods that were used to measure the drag on the ellipsoid body.

1.3 Organization of Thesis

The remainder of this thesis is organized as follows: Chapter 2 describes the experimental apparatus used in this study. Included in the chapter is a description of the Virginia Tech Stability Wind Tunnel, the design and construction process behind the

ellipsoid model, a description of the seven-hole probe and associated pressure sensing equipment, information about the traverse used to move the probe in the wake of the model, and details about the data acquisition system used in the testing.

Chapter 3 discusses the methods used in the testing. First, a detailed explanation of the experimental setup is given. This includes how the model was setup and positioned in the wind tunnel as well as the arrangement of the seven-hole probe, traverse, and testing equipment. Next, the test procedure is discussed followed by the steps necessary to reduce the data and perform drag, circulation, and lift calculations on the model.

Chapter 4 presents the results of the study. Figures are presented that show the wake profiles, some of the secondary flow profiles, and some of the stream-wise vorticity profiles of the test cases that were performed. Then the results of the drag, circulation, and lift are shown and discussed. Finally, uncertainties in the data and calculations are given and explained in context with their effects on the results.

Chapter 5 summarizes the study and formulates conclusions based on the results seen in Chapter 4. References and a personal vita follow the conclusions at the end of the paper.

2 Experimental Apparatus

2.1 Wind Tunnel

2.1.1 Wind Tunnel Background

All tests were conducted in the Virginia Tech Stability Wind Tunnel. The tunnel was built in 1940 by the NACA Langley Aeronautical Laboratory to determine dynamic stability derivatives of models in a fixed position; hence the name "Stability Wind Tunnel." The tunnel was acquired by Virginia Tech in 1958 and re-constructed in its current location next to Randolph Hall. After three years of calibration, the tunnel became operational in 1961. In 1994 the fan motor was completely overhauled and the windings were reinsulated; two years later new fan blades were acquired to improve the overall tunnel efficiency. Figure 2.1 shows a picture of the tunnel outside of Randolph Hall (Stability Wind Tunnel, 2007).

Figure 2.1: Outside View of the Virginia Tech Stability Wind Tunnel

2.1.2 Wind Tunnel Description

The tunnel is a continuous, closed jet, single return, subsonic wind tunnel with an interchangeable test section measuring 7.3 m long and 1.83 m high and wide. The test section is enclosed on two sides by glass walls that provide optimum viewing of the test model from the control platform that surrounds the outside of the test section. The tunnel is powered by a 0.45-MW variable speed DC motor that can drive a 4.3 m propeller up to 600 RPM. This provides a maximum speed of about 80 m/s and a Reynolds number of 5.45 million per meter in the tunnel test section (Stability Wind Tunnel, 2007).

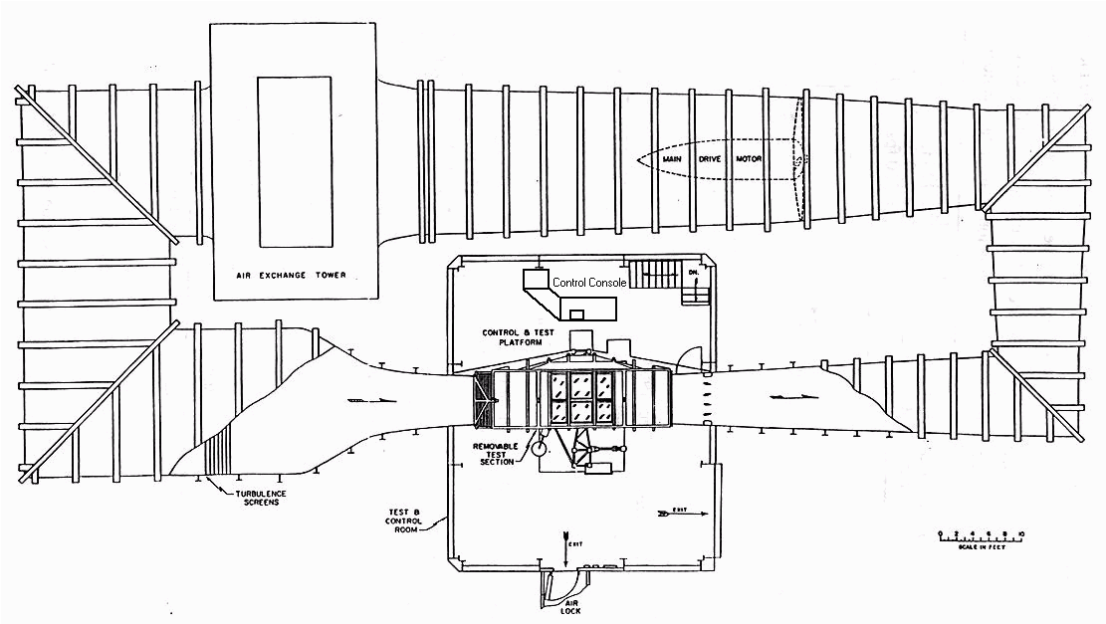

Figure 2.2: Schematic of Virginia Tech Stability Wind Tunnel

Tunnel speed and conditions can be precisely adjusted and monitored by a custom designed Emerson VIP ES-6600 SCR Drive, which was installed in 1986. The precisely regulated DC power source eliminates all of the cyclic unsteadiness in tunnel velocities commonly found with older tunnel drive systems as well as the turbulence inducing vibrations inherent with such drive systems. Overall flow uniformity in the tunnel is very good. Turbulence levels are low; Choi and Simpson (1987) report that they

are on the order of 0.05% and vary with the flow speed, with higher velocities producing the highest fluctuations. More recent measurements that have not yet been published have shown that tunnel turbulence levels are now significantly lower than 0.05%. Although not originally designed as a low turbulence facility, the addition of seven anti-turbulence screens, coupled with the other flow smoothing features of the tunnel, result in very low turbulence levels (Stability Wind Tunnel, 2007).

2.2 Ellipsoid Model

2.2.1 Model Description

The wind tunnel model used in this study was built to a length of 1.6 m, a width of 0.4 m, and a height of 0.231 m. The model consists of three pieces, a 0.4 m bow and stern and a 0.8 m mid-section. The model itself is not a true ellipsoid but is a scalene ellipsoid split in two by a cylinder with a constant oblate ellipse cross-section. However, since the cross-section of the model always takes the form of an oblate ellipse, it has been dubbed the "oblate ellipsoid model" and is always referred to as such in this paper.

The bow and stern pieces are identical and if connected together would form the two halves of the scalene ellipsoid. This scalene ellipsoid would have a total length of 0.8 m, a maximum width of 0.4 m, and a maximum height of 0.231 m. Thus, the cross-section of the bow and stern is an oblate ellipse that gradually increases in size to 0.4 x 0.231 m, when moving from the nose to the intersection with the mid-section. The mid-section of the model is a 0.8 m long cylinder and has the same cross-section as the bow and stern pieces (0.4 x 0.231 m), so that the transition moving along the surface from the

bow to the mid-section and from the mid-section to the stern has no curvature discontinuities. Figure 2.3 shows a schematic of the model.

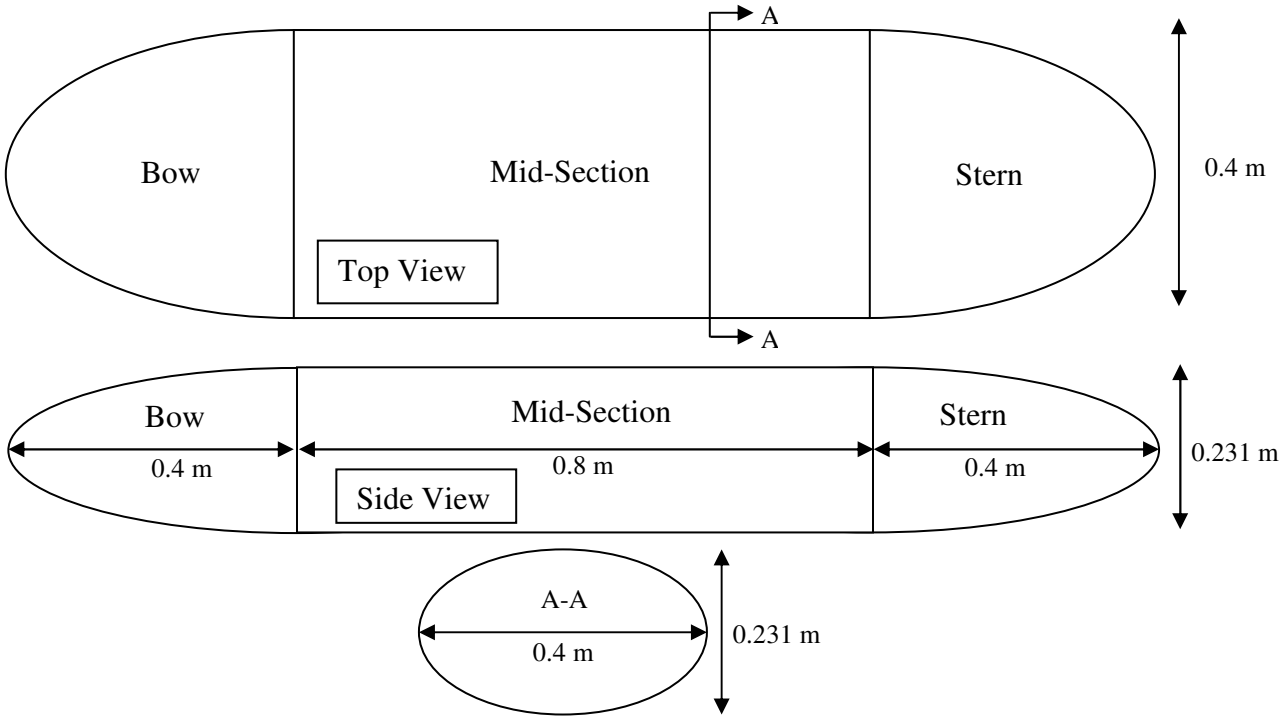

Figure 2.3: Schematic of the Ellipsoid Model

2.2.2 Overview of the Construction Process

The ellipsoid model was built in-house following the construction techniques developed for the Suboff model that are described by Whitfield (1999), Granlund (2004), and Simpson (2002). Like the ellipsoid, the Suboff model was constructed from similar composite materials, but took the shape of a standard constant circular cross-section submarine model. The basic construction procedure was to use computer blueprints to build a foam male plug of the model. The plug was then used to construct a female fiberglass mold. Finally, composite materials were used in the mold to form the two separate halves of the model that would be glued together.

2.2.3 Male Plug Construction

The construction process began by generating a computer model to the specifications given by the schematic in Figure 2.3. Full-size drawings of the model's cross-sections, spaced every two inches, were then printed out. These drawings were pasted to 2" inch thick extruded polystyrene board so that each cross-section could be cut out with a scroll saw (Figure 2.4).

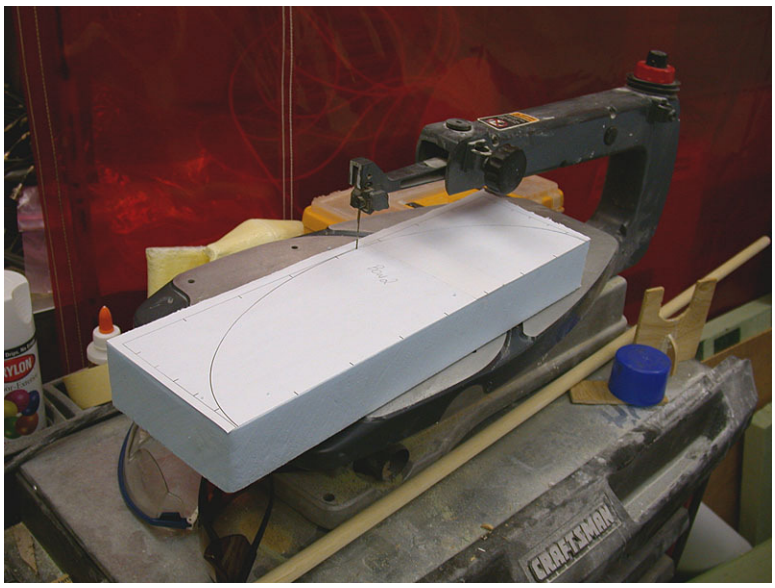

Figure 2.4: Cutting Out Foam Cross-Sections

When all the foam cross-sections had been cut out, they were glued together with 5-minute epoxy to form a rough approximation of the male plug. Beginning with coarse 80-grit and then fine 220-grit sandpaper, the foam plug was carefully sanded into its proper shape. When the sanding was complete, a thin fiberglass weave cloth was draped over the plug and a layer of epoxy was applied over it. This completely soaked the weave and allowed it to be adhered tightly to the foam surface. The next step in the construction of the plug involved coating the entire surface with Bondo and gradually sanding it down with finer and finer sandpaper until the surface felt completely smooth to

the touch. With this done, the plug was glued to a Plexiglas sheet with 5-minute epoxy and four layers of non-silicone, non-polymer wax were applied to the surface and buffed out. Finally, a layer of polyvinyl alcohol was sprayed over the surface and allowed to dry, completing the construction of the plug. Figure 2.5 shows the various steps of the construction of the plug (Granlund, 2007).

Figure 2.5: (Top Left) Gluing the Cross-Sections Together, (Top Right) Sanding the Plug to Its Proper Shape, (Bottom Left) Adhering the Fiberglass Weave to the Foam, (Bottom Right) The Finished Plug after Applying the Polyvinyl Alcohol Layer

2.2.4 Female Mold Construction

The completed male plug was used to create a female mold of fiberglass reinforced epoxy. First, a small clay knob was formed and placed on the male plug; when the mold was finished, the knob would be removed leaving a hole in the mold.

This hole would then allow for compressed air to be directed into the mold so that it could be separated from the male plug or later on, the model itself. Next, the mold surface coat was created by spreading Fibre Glast #1099 Epoxy Surface Coat over the plug. Two layers of 6oz. fiberglass weave, followed by a thick layer of 20oz. weave, and then two more layers of 6oz weave were epoxied over top of the mold surface coat. To obtain sufficient twisting stiffness, a layer of quarter-inch over-expanded Nomex honeycomb and an outer layer of 6oz. weave were then added on top of the first five layers of weave to complete the mold. Figure 2.6 summarizes the mold construction steps (Granlund, 2007).

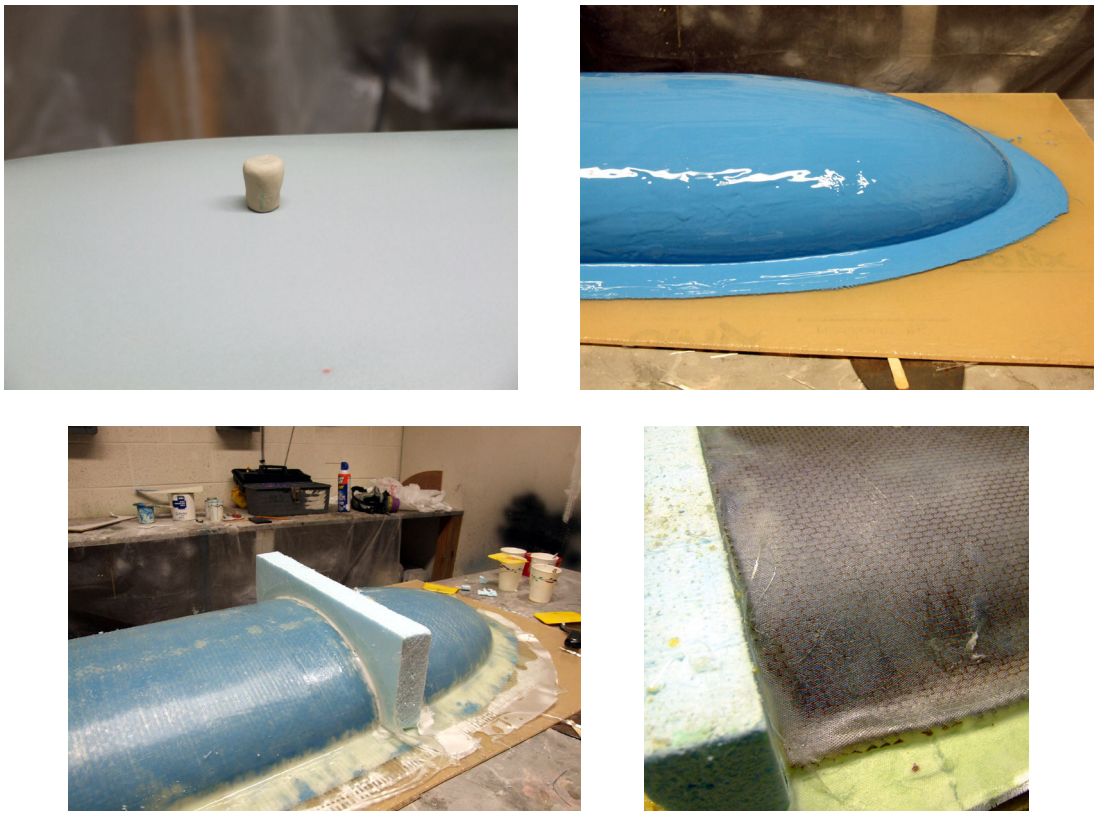

Figure 2.6: (Top Left) Applying the Clay Knob to the Plug, (Top Right) Applying the Mold Surface Coat, (Bottom Left) Adhering the Five Layers of Fiberglass Weave to the Mold, (Bottom Right) The Final Layers of Honeycomb and Weave

When the epoxied layers had cured, the mold was separated from the plug by attaching a compressed air hose to the hole that was created by removing the clay knob and by turning on the air. The inside of the mold surface was then sanded with very fine grit paper and polished with Fibre Glast mold polish, machine glaze, and four layers of carnauba wax. The mold was now ready to create the model (Granlund, 2007).

2.2.5 Model Construction

With the mold completed, the model could be formed by creating two separate halves from composite materials and gluing them together. To start this process, an epoxy surface base coat was applied to the mold. Then a layer of 3K 2x2 twill carbon fiber weave was laid over top of the base coat and another application of epoxy was spread out over the weave. This layer was covered with nylon peel-ply, breather cloth, and a vacuum bag. A vacuum hose was attached to the bag and the vacuum pump was started and allowed to run for several hours while the epoxy cured. Afterwards, the vacuum bag, breather cloth and nylon peel-ply were removed. Another layer of epoxy was then put on followed by a layer of honeycomb. For the mid-section of the model, Hexcel HRH-10-F35-2.5 honeycomb was used. Hexcel HRH-36-F50-2.0 honeycomb was employed for the double curvature surfaces of the bow and stern. The vacuum curing process was then repeated over the honeycomb. When that had finished, a final layer of epoxy and twill carbon fiber weave were laid over top of the honeycomb and the vacuum curing process was repeated again. When finished, the compressed air hose was attached to the small hole in the mold and the model half was popped loose. This process was then repeated for the other half of the model. Figure 2.7 shows some pictures from this part of the construction (Granlund, 2007).

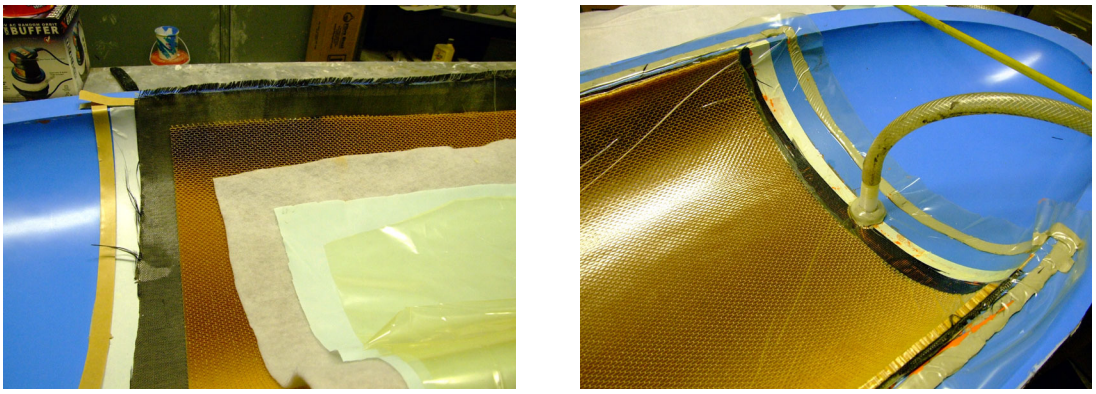

Figure 2.7: (Left) Materials Used in the Construction, (Right) Vacuum Bag Curing

Before the two halves of the model were glued together, two 1/8" thick aluminum rings were mounted inside the model at the fore and aft-most points of the constant cross-section mid-section. In order to obtain access to the inside of the model, the mid-section of the top half was cut out and made into a hatch that could be attached from the outside with bolts through the aluminum rings. Finished with red paint on the hatch and black paint over the rest of the surface, the model weighs 2.56 kg and is rigid. Total uncertainties in the dimensions of the model are approximately 0.1% in length, 0.4% in width and 0.6% in height (Granlund, 2007). Figure 2.8 shows the finished model.

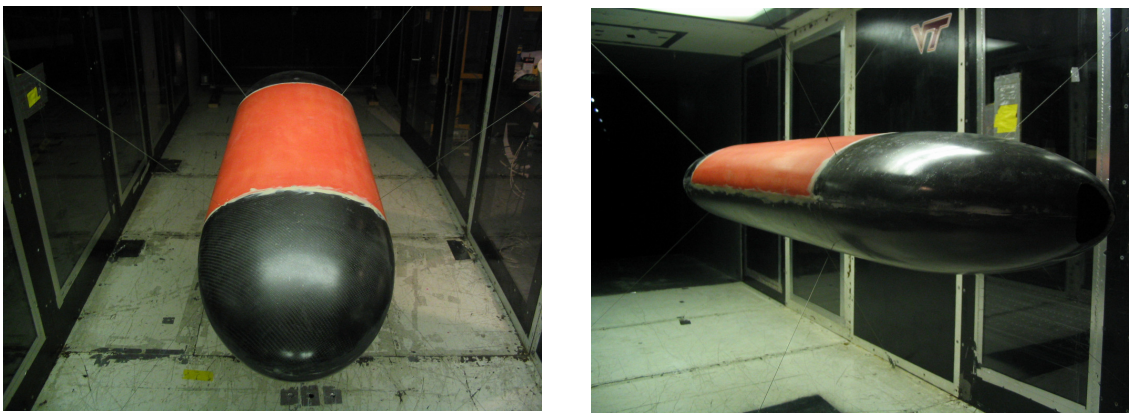

Figure 2.8: Two Views of the Completed Model

2.3 Seven-hole Probe

2.3.1 Probe Description

The seven-hole probe (Figure 2.9) that was used in this study was a S7TC-317-152 model manufactured by Aeroprobe Corporation in Blacksburg, VA. It has a 15.2 cm long stem and a 3.17 mm diameter with seven tubes having an internal diameter of 0.5 mm imbedded in the stem. The probe has a cone frustum tip with a half angle of 30°. Six of the pressure ports (numbers 2 through 6) are equally distributed in 60° increments around the tip, while the first port is located at the tip of the probe (Pisterman, 2004).

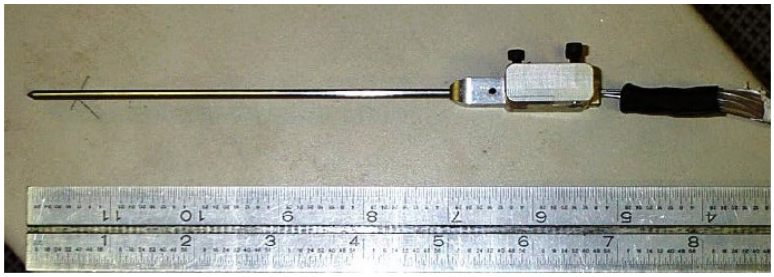

Figure 2.9: Seven-Hole Probe (Adapted from Pisterman, 2004)

2.3.2 Pressure Transducer Box

To determine the pressures from the probe, seven Tygon tubes of 1/16 inch internal diameter were run from the probe to a transducer box containing seven Data Instruments Model XPCL04DTC pressure transducers. Each transducer has a ±2.5 inch of water range and is temperature compensated over a 0-50°C range. The volume of the transducers' differential pressure ports are 0.004303 inch³ and 0.003908 inch³. The transducers operated in differential mode and used the Stability Tunnel's free-stream static pressure, obtained via a Pitot-static probe, as a reference pressure.

The transducers' output signal is ±25 mV and needs to be amplified to an appropriate range for data acquisition. To do this, a Burr-Brown Model INA131AP 100-

gain amplifier was used as well as a low-pass filter with a 200 Hz cutoff frequency to reduce the noise of the signals. The transducer signals coming out of the box were input to a PC via a 16-bit resolution Data Instruments PCI-6013 data acquisition card with a CB-68LP connector bloc allowing up to eight simultaneous inputs with a total sampling rate of 200,000 samples per second.

An Omega 5 type K precision fine wire thermocouple was used to sense the temperature inside the transducer box with an uncertainty of ±0.5°C. It also sent its signals to the PC via a National Instruments SCB-68 card. To limit the temperature variations of the seven pressure transducers, the transducer box was insulated with a one-inch thick layer of Styrofoam. A Tektronix CP5250 power supply provided 11V to the transducer box to power the transducers (Pisterman, 2004).

2.3.3 Probe Calibration and Data Reduction

To understand the details behind the seven-hole probe's calibration, it is first necessary to describe the data reduction algorithm that allows for the determination of pressures and velocities from the probe. Johansen, et al (2001) developed and discussed the data reduction algorithm and it is also summarized by Pisterman (2004).

The flow properties measured by the seven-hole probe are determined by two sets of pressure coefficient equations corresponding to low and high flow incidence angles with respect to the probe. This is necessary because the probe can perform measurements over a wide range of flow angles; high incidence angles can cause the flow to separate on the leeside of the probe, rendering pressure ports in those regions useless. In these situations, the maximum pressure is read by one of the probe's circumferential pressure ports, and only the ports located in non-separated flow regions are used in the data

reduction algorithm. For low incidence angles, when the port located on the tip of the probe reads the maximum pressure, the flow is attached everywhere on the probe surface and all of the pressure ports are used in the data reduction algorithm. Thus, the following equations from Johansen, et al (2001) define a pseudo-dynamic pressure (q) and a set of non-dimensional pressure coefficients (b_1, b_2, A_t, A_s) from the pressure readings of the probe's seven pressure ports (P_1 through P_7), the total pressure (P_t), and the static pressure (P). For low incidence angles, the equations are given as:

$$\begin{aligned} q &= P_1 - \frac{P_2 + P_3 + P_4 + P_5 + P_6 + P_7}{6} \\ b_1 &= \frac{P_5 + P_4 - P_7 - P_2}{q\sqrt{3}}, \quad b_2 = \frac{P_2 + P_4 - P_7 - P_5}{2q} + \frac{P_3 - P_6}{q} \\ A_t &= \frac{P_1 - P_t}{q}, \quad A_s = \frac{q}{P_t - P} \end{aligned} \tag{1}$$

Then for high incidence angles, the equations become:

$$\begin{aligned} q &= P_{i\max} - \frac{P^+ - P^-}{2} \\ b_1 &= \frac{P_{i\max} - P_1}{q}, \quad b_2 = \frac{P^+ - P^-}{q} \\ A_t &= \frac{P_{i\max} - P_t}{q}, \quad A_s = \frac{q}{P_t - P} \end{aligned} \tag{2}$$

where $P_{i\max}$ is the pressure from the port that reads the maximum pressure and P^+ and P^- are the pressures from the ports located immediately clockwise and counter-clockwise from the maximum port.

The seven-hole probe and pressure transducers were calibrated at the Aeroprobe Corporation's facilities in Blacksburg several years prior to this study. The probe was placed in a low turbulence intensity steady uniform known flow-field. By changing the pitch (α) and yaw (β) angles of the probe with respect to the flow-field, a calibration

database consisting of the pressures from each of the seven pressure ports, the pitch and yaw flow angles, the total and static pressures, and the calculated non-dimensional pressure coefficients (b_1, b_2, A_t, A_s) were obtained. Additionally, the pressure/voltage conversion values for the seven pressure transducers were obtained during the calibration.

The transducer results from the calibration were used in a Matlab program that was jointly developed by Pisterman and Aeroprobe to translate the voltage signals from the probe's pressure traducers into pressure readings after data had been collected. These results and the calibration database could then be read into Multiprobe v.3.3.1.240, a software package for the seven-hole probe that was developed by the Aeroprobe Corporation to calculate all of the flow properties using Johansen's data reduction algorithm that is further discussed below.

In Multiprobe, the sets of non-dimensional pressure coefficients from the calibration database that are similar to the sets of non-dimensional pressure coefficients calculated in an unknown flow-field are used to interpolate the flow properties in that flow-field via a first order polynomial fit:

$$\begin{aligned} \alpha &= \alpha(b_1, b_2) = c_{0\alpha} + c_{1\alpha} b_1 + c_{2\alpha} b_2 \\ \beta &= \beta(b_1, b_2) = c_{0\beta} + c_{1\beta} b_1 + c_{2\beta} b_2 \\ A_s &= A_s(b_1, b_2) = c_{0As} + c_{1As} b_1 + c_{2As} b_2 \\ A_t &= A_t(b_1, b_2) = c_{0At} + c_{1At} b_1 + c_{2At} b_2 \end{aligned} \tag{3}$$

where c_{0j}, c_{1j}, and c_{2j} are the polynomial coefficients ($j = \alpha$, β, As, or At). With the values from Equation 3 known and the total temperature (T_t) from the flow-field given, the total pressure, static pressure, Mach number (M), flow temperature (T), and the magnitude of the velocity vector, $\left\|\vec{U}\right\|$, can be determined by the following equations from Johansen, et al (2001):

$$P_t = P_{i\max} - qA_t \tag{4}$$

$$P = P_t - \frac{q}{A_s} \tag{5}$$

$$M = \sqrt{5\left[\left(\frac{P_t}{P}\right)^{2/7} - 1\right]} \tag{6}$$

$$T = \frac{T_t}{\left(1 + M^2/5\right)} \tag{7}$$

$$\left\|\vec{U}\right\| = M\sqrt{\gamma RT} \tag{8}$$

where γ is the ratio of specific heats. Finally, the three components of the flow velocity (U, V, W) can be determined from:

$$\begin{aligned} U &= \left\|\vec{U}\right\|\cos(\alpha)\cos(\beta) \\ V &= \left\|\vec{U}\right\|\sin(\alpha)\cos(\beta) \\ W &= \left\|\vec{U}\right\|\sin(\beta) \end{aligned} \tag{9}$$

Pisterman (2004) compared the velocity measurements made by the probe and its current calibration with measurements from a hot-wire and a laser Doppler velocimeter (LDV), which had reported uncertainties of ±1% and ±0.26%, respectively. In the comparisons, the probe measurements differed by less than 0.5% from the hot-wire and LDV measurements in a quasi-steady, non-turbulent flow field with low velocity gradients and by around 1.5% in complex flow fields with large turbulent kinetic energy and unknown velocity gradients. Since the methods and equipment used by Pisterman (2004) were nearly identical to the ones for this study, overall uncertainty in the probe velocity measurements are assumed to be at the same level as those reported by Pisterman.

2.4 Traverse

To make wake surveys in the tunnel, the seven-hole probe was mounted to a two-axis traverse (Figure 2.10) that was positioned at the back of the wind tunnel test section.

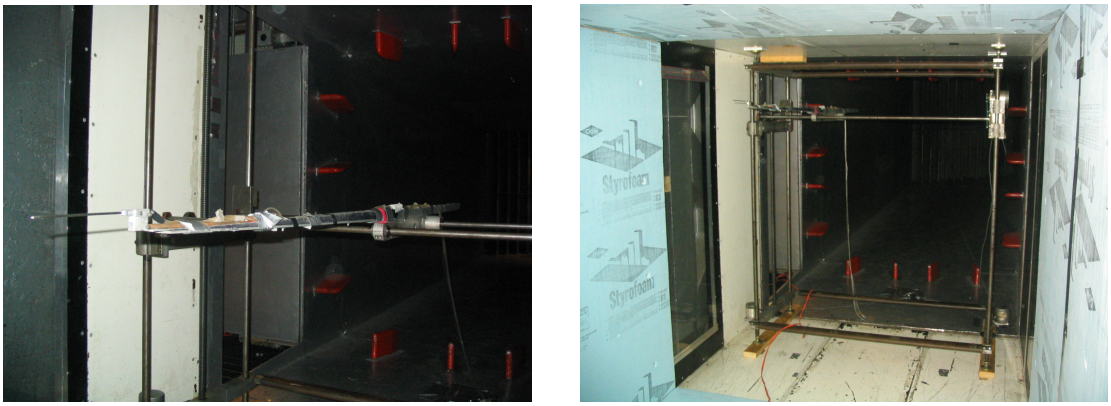

Figure 2.10: (Left) Probe Mounted on the Traverse, (Right) Two-axis Traverse

The traverse consists of three Compumotor Model 083093-1-8-040-010 stepper motors, three rotating motion screws, six sliding rods for a sting to move on, and a support structure to hold everything in place. The probe was securely mounted to a sturdy aluminum sting that extended 0.76 m from the traverse. The sting was fixed to two horizontal sliding rods and the horizontal motion screw, which was driven by the first stepper motor. A bar on each end of the horizontal rods and screw attached them to the two vertical axes (one on each side) of the traverse. Four stationary horizontal beams (two placed on the top and two on the bottom) connected the two vertical axes together and provided support. Each vertical axis consisted of two sliding rods and a motion screw. Two stepper motors operated in sync on either side of the traverse and drove the two vertical motion screws, which moved the horizontal axis and sting up and down. In this way the seven-hole probe could be traversed to any vertical or horizontal location with an uncertainty of 0.025 mm (Zsoldos, 1992). However, its position was fixed along the axis of the flow direction.

To mount the traverse in the tunnel test section, each vertical axis sliding bar contained an adjustable foot on each end. Thus, there were four feet on the top and bottom of the traverse that could be extended outward to wedge the traverse between the top and bottom walls of the test section. Since the feet could not extend all the way to the two walls, small 2x4's were inserted between the walls and the feet to make up the difference. With the feet fully tightened, the traverse became firmly wedged in the tunnel and did not vibrate with the wind on.

The traverse could be operated externally from the data acquisition PC, which could send commands via a serial connection to the three Compumotor Model SC32/RS2320 motor controller boxes, which in turn passed the signal onto the traverse stepper motors. To ensure smooth operation, all moving components of the traverse were lubed with WD-40 each day during the testing period. This helped to prevent any of the motor gears from skipping.

2.5 Data Acquisition System

The data acquisition and the traverse operation were done with a Labview code on a PC. Once started, the code could collect the data autonomously. The code works by ordering the traverse to move the seven-hole probe from position to position on a predetermined grid to survey the wake of the ellipsoid model. At each point, the probe takes a set number of samples at a set sample rate before moving to the next point in the grid. The code records all of the pressure and temperature signals sent from the transducer box in several text files. The Labview code was initially developed by Pisterman, but it had to undergo significant modifications that included incorporating the

movement of the probe on the traverse that was used in this study. More information about the data acquisition, sample rate, sample time, grid sizes and operation procedure is given in Sections 3.2.1 and 3.2.2.

After finishing a survey grid, the pressure and temperature text files that had been stored by the Labview code were sent to the Matlab reduction code that had been previously developed by Pisterman and Aeroprobe. The code used the manufacturer's calibration data to determine the pressures read by the probe at each point from the sample voltages that were acquired. All of the data averaging in this study was performed in this code as pressure measurements at each grid point were obtained by averaging over the total number of samples for each point.

Finally, the velocity, pressure, temperature, density, and rotation angles of the flow at each point were calculated using Multiprobe v.3.3.1.240. This required an input of the tunnel total temperature during testing (measured from the tunnel control station) along with the pressure results from Matlab. This data file could then be used to perform the drag analysis and lift analysis, which is discussed later. Figure 2.11 shows a picture of the data acquisition station outside of the tunnel test section. The blue box located to the left of the computer monitors is the tunnel control box.

Figure 2.11: Data Acquisition and Tunnel Control Station, with NNEMO Model in Background

3 Methods

3.1 Experimental Setup

3.1.1 Tunnel Coordinate System

Indicated in Figure 3.1 is the tunnel coordinate system. The x-axis is oriented in the positive stream-wise direction. The y-axis is normal to the tunnel floor and positive in the up-direction. The z-axis covers the span-wise direction and completes the tri-diagonal system. For reference, the x-axis origin is located at the leading edge of the model.

3.1.2 Setup in the Test Section

Also shown in Figure 3.1 is a side-view schematic of the drag test setup for all tests in the Stability Wind Tunnel test section. In the figure, flow is from right to left and the model is attached to the top and bottom walls by eight guy wires, four in each axial plane. The traverse is set back at the far end of the test section with the seven-hole probe mounted to its sting.

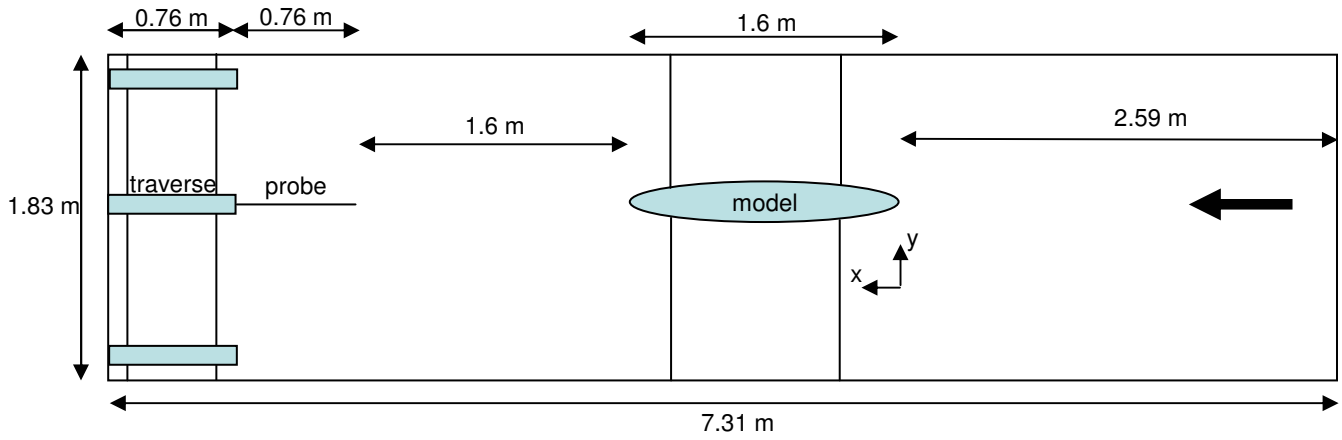

Figure 3.1: Drag Test Setup

The setup for the tests was governed primarily by the need to have enough space between the probe tip and trailing edge of the model. Barlow, et al (1999) suggests that wake pressure surveys need to be conducted at least 0.7 chord lengths behind the trailing edge of the model so that the wake static pressure can return to a uniform downstream tunnel static pressure. To accomplish this, the traverse and probe were setup as far back as possible in the test section and the model was mounted one chord length (1.6 m) upstream of the probe tip. Data taken from the seven-hole probe show that over the typical two hour survey time, the static pressure coefficient was generally uniform with variations of no more than 0.01 across the free-stream regions of the wake survey area for all test cases. Figure 3.2 shows the typical static pressure coefficient variation; here the model was mounted at 0° angle of attack with trips in test case #1.

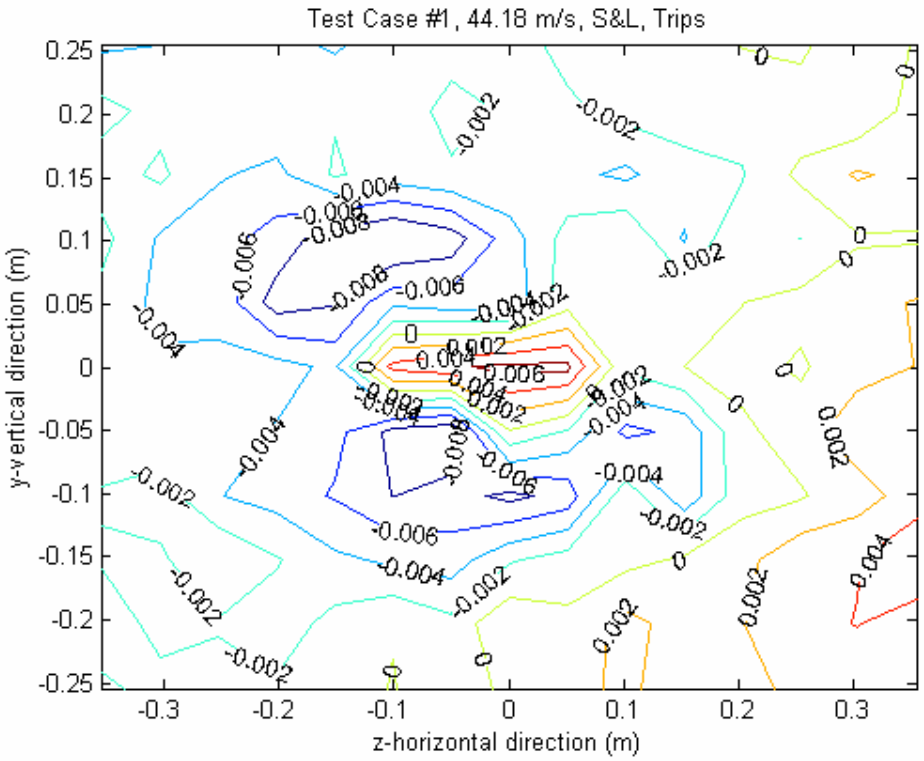

Figure 3.2: Test Case #1, Static Pressure Coefficient Variation in the Wake Survey Region

The test setup positioned the center of the model 3.39 m downstream of the test section inlet, which is nearly the center of the test section. In the y-z span-wise plane, care was taken to ensure that the longitudinal axis of the model was lined up in the center of the tunnel. A digital inclinometer was used to ensure that the model was mounted at the proper angle of attack with no roll or yaw to an uncertainty of ±0.1°; measurements were made from the model surface to the tunnel walls to ensure that the model was positioned in the center of the tunnel to an uncertainty of about ±1 cm.

3.1.3 Setup of Other Equipment

The cables connecting the transverse motors to the traverse controller boxes and the seven Tygon tubes running from the seven-hole probe to the transducer box were run from the traverse through a small hole in the floor of the tunnel diffuser. To ensure that the cables and tubes did not flap about too much in the wind, tie-wraps were used to bundle them together; the bundles were then taped to the traverse and diffuser floor in appropriate locations to secure them. The cables and tubes then came outside the tunnel and ran to the traverse controller boxes and transducer box, which were positioned on the floor of the tunnel control platform. Signals were then sent from the controller boxes and the transducer box via cables to the data acquisition (DAQ) computer that was placed on a table a short distance away.

3.1.4 Guy Wire Suspension of the Model

The model was designed to be suspended by guy-wires attached to the tunnel test section during testing. This enables drag tests to be conducted using wake surveys since there is no bulky support structure creating a wake coinciding with that of the model.

The guy wires were located on the model at positions where the pressure gradients were favorable; thus they did not induce separation on the model. Additionally, because of their position in the free-stream flow, the wire wakes could easily be accounted for and eliminated when analyzing the wake survey data. Thus, holes were drilled into the model and through the aluminum support rings to attach the guy wires to the inside of the model. The other ends of the guy wires were connected to turnbuckles that could screw into the test section walls and be used to adjust the model's position in the tunnel.

Several different wire configurations were tested on the model before arriving at the final configuration. Initially, six guy wires were used; three were mounted at the forward line of the center hatch, while the others were mounted at the aft line of the hatch. For the forward and aft wire sets, two wires came out of the bottom of the model and one came out the top in an inverted Y configuration. However, this configuration proved problematic as the model position could not be adjusted adequately.

In an attempt to fix this problem, the downstream set of guy wires was modified to an upright Y configuration, while the forward wires were left in the inverted Y configuration. This permitted better adjustment of the model's position but did not provide adequate support and stability; the model had a slight vibration to it when the wind was turned on.

Finally, it was decided to use eight guy wires in an X configuration at both the forward and aft lines of the center hatch. This provided the best adjustability, support, and stability of all of the wire configurations. When the turnbuckles were fully tightened, the model became solidly fixed in place and had no vibration issues. Figure 3.3 shows the model mounted in the test section in the X wire configuration.

Figure 3.3: Model Mounted in Tunnel with the X Guy Wire Configuration

3.1.5 Laminar/Turbulent Transition Trips

Some test cases required the use of trip strips to transition the flow on the model surface. There were two methods available to accomplish this: post trips and grit tape trips. However, time constraints in the tests allowed for only one method to be used. Previous experience using both the post and grit tape trips in the NNEMO model drag tests indicated that the difference in the results between the two methods were practically negligible. Thus, grit tape trips were used on the ellipsoid model's surface due to their easy and timely method of application.

The idea behind using grip tape trips came from their use in another drag study on the NNEMO model by the researchers from Old Dominion University using the Langley

Full-Scale Tunnel at the NASA Langley Research Center. The trips for the Langley tests were identical to the ones employed here. Pieces of 3M Safety-Walk Step and Ladder 7634 NA grit tape were cut into 6.35 mm wide strips and pinked with triangle pinking shears on the leading edge. The tape trips were then staggered on top of one another as shown in Figure 3.4 (Note the model in the picture is the NNEMO).

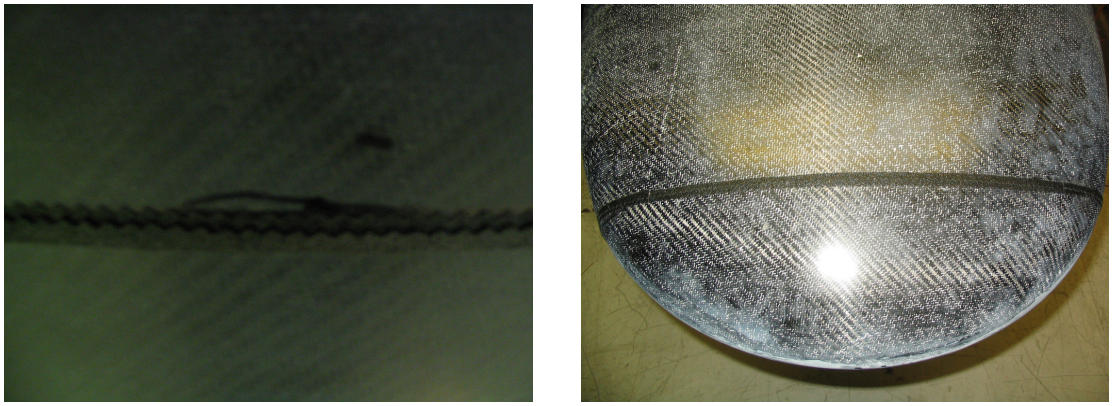

Figure 3.4: Grit Tape Trip Configuration on the Model

Before the trips could be applied, an analysis was done to determine where they should be placed on the model. There are three driving factors behind the trip placement. First, the trips should be located far enough back on the model where a sufficiently high Reynolds number is present so that the tripped flow does not undergo relaminarization. To determine this location, a relaminarization factor (k) was calculated at different stations along the model. Schetz (1993) gives the following equation for the relaminarization factor:

$$k = \frac{\nu_e}{U_e^2}\frac{dU_e}{dx} \tag{10}$$

where ν_e is the edge kinematic viscosity and U_e is the boundary layer edge velocity. If k is greater than 2 x 10^{-6}, relaminarization can occur, so the trip location should be at model stations where k is less than 2 x 10^{-6}. To find values for k at different model stations, U_e

was calculated over the model at a 0° angle of attack using an inviscid vortex panel method based on a free-stream velocity of 44 m/s and 16 m/s; the value of the viscosity was assumed to be 1.533 x 10^{-5} m^2/s. Figure 3.5 shows the value of *k* at various stations along the model. The relaminarization limit is marked by the red line on the figure and indicates that the trips should be placed at an *x/L* model station of 0.05 or greater, since at 16 m/s the flow can become laminar again upstream of this point.

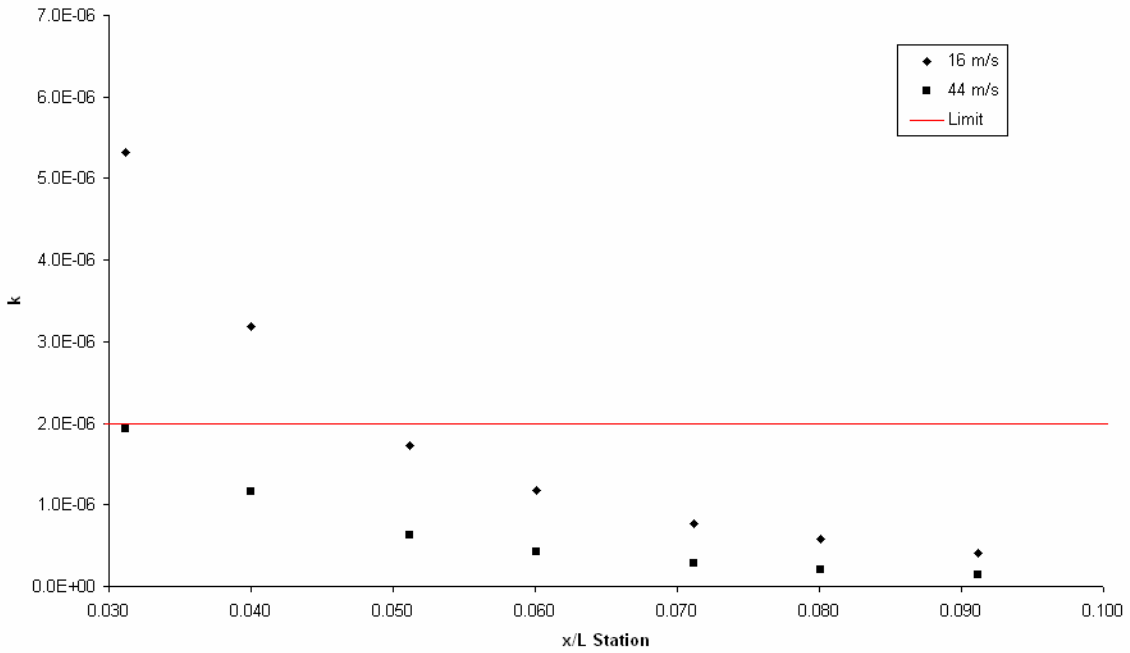

Figure 3.5: **Relaminarization Factor along the Model Surface**

The second factor in determining the trip location is that the momentum loss by the trips should be sufficient to produce a turbulent momentum thickness Reynolds number. Fussell and Simpson (2000) state that transition to turbulent flow occurs if the trips can cause a change of 800 or greater in the momentum thickness Reynolds number. Following Fussell's analysis, the change in momentum thickness Reynolds number was calculated for several possible trip locations along the model's surface. The results are shown in Figure 3.6 and indicate that the trips could work at any *x/L* station since they

always produce a large enough change (denoted by the red line) in the momentum thickness Reynolds number.

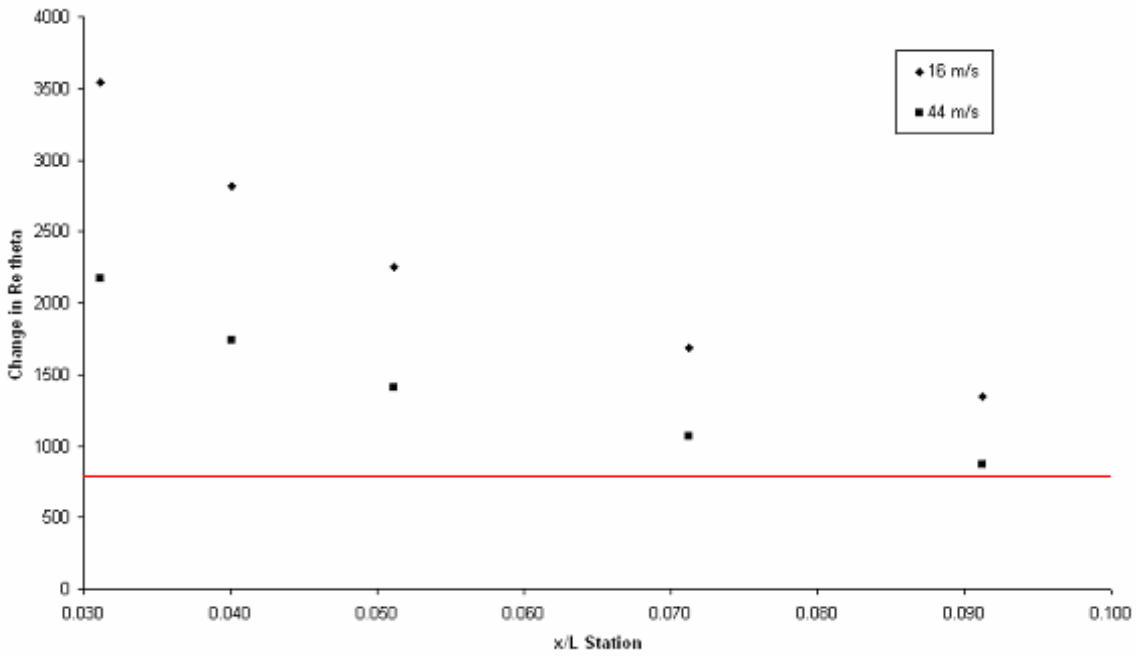

Figure 3.6: Change in Momentum Thickness Reynolds Number at Various Trip Locations

The last factor makes sure that the trips are not too far downstream so that they are placed outside of the favorable pressure gradient zone for all possible model alignments with the flow. This factor is important since trips in adverse or positive pressure gradient regions can induce separation, which may become unstable or unsteady. Prior to testing, it was determined that no data would be taken with the model above a 20° angle of attack. Thus, a 20° tangent line was drawn on a side profile drawing of the model (Figure 3.7). The trips should be placed below the line's intersection point with the bow to ensure that they are in a favorable pressure gradient zone at all times. Figure 3.7 indicates the trips should be placed no further back than an x/L of 0.06.

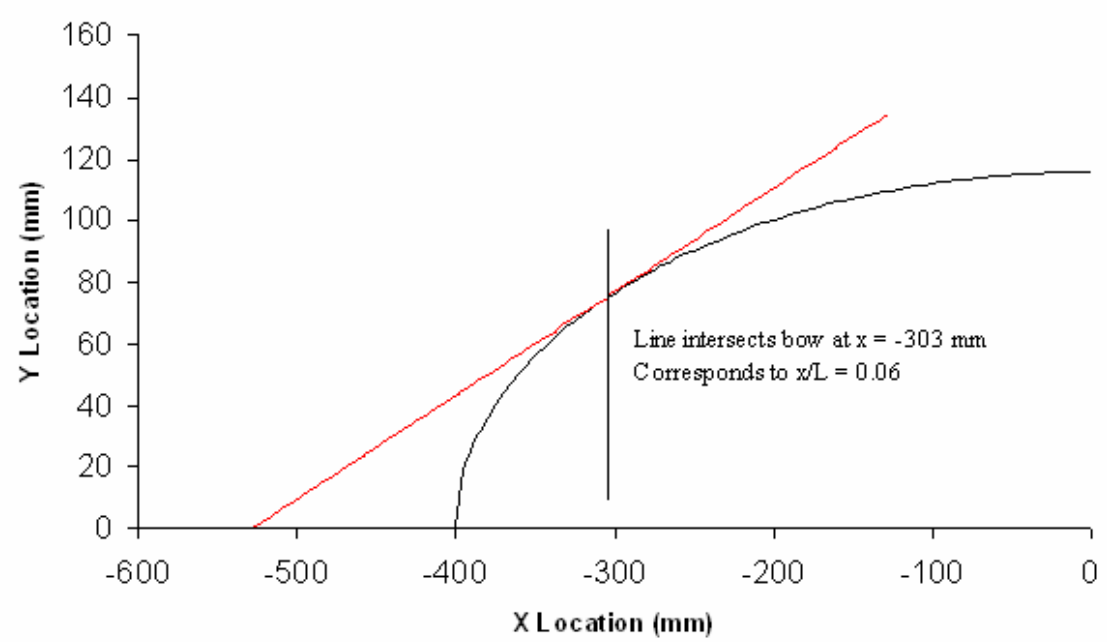

Figure 3.7: Intersection of 20 Degree Tangent Line with Model Surface

When taking all three of the factors into account, a narrow window of trip strip placement was revealed on the model. The first and third factor mandated that the trips be located somewhere between $x/L = 0.05$ and 0.06. For these reasons, the trip location was set at $x/L = 0.05$.

3.1.6 Test Cases

As mentioned by the Introduction, only five drag tests were conducted on the ellipsoid model due to its secondary priority and time constraints. All drag tests were conducted following the setup described in Section 3.1; Table 3.1 lists all of the test cases. In future sections of this thesis, the test cases will be referred to by number instead of writing out their full name.

0° Angle of Attack Test Cases
#1: 44 m/s Free-stream Velocity, Trips Applied
#2: 44 m/s Free-stream Velocity, No Trips Applied
10° Angle of Attack Test Cases
#3: 44 m/s Free-stream Velocity, Trips Applied
#4: 44 m/s Free-stream Velocity, No Trips Applied
#5: 16 m/s Free-stream Velocity, No Trips Applied

Table 3.1: Drag Test Cases

3.2 Test Procedure

3.2.1 Preparation before Running the Tunnel

After the model and test equipment were installed in the tunnel, preparation for data collection could begin. Several things had to be done before the tunnel could be started. First, the pressure transducers and traverse motors were turned on and warmed up for 30 minutes to stabilize any transducer drift and prevent any motor errors. While this took place, the Labview data acquisition program on the DAQ PC was brought up and initialized with several key pieces of information.

The grid for the probe survey was the first thing that had to be loaded into the Labview data acquisition program. The grid was designed to capture the entire wake of the model and the adjacent free-stream in order to provide a baseline from which to calculate the drag. For this reason, the grids at the two model angles of attack differed.

For all test cases, the grid origin ($y = z = 0$ m) was located along the tunnel center-line. For the 0° test cases, the grid was centered at the origin. Grid points were specified up to 0.2540 m above and below the origin and 0.3556 m to the left and right of the origin. The increment for each grid point was 0.0508 m in both the vertical and

horizontal directions. For the 10° test cases, the grid was centered below the tunnel center-line at y = -0.0508 m and z = 0 m, since the wake had shifted downwards. Grid points were equally spaced between y = 0.2540 m and y = -0.4064 m in the vertical range and 0.4572 m to the left and right of the origin. The increment for each grid point was 0.0508 m in both the vertical and horizontal directions.

Next, the sample size (1000 samples per grid point for all test cases) and sample rate had to be entered into the Labview data acquisition program. To find the sample rate, the total sample time (t) for the probe at a grid point had to be calculated from the following equation:

$$t = \frac{200L}{U_\infty} \tag{11}$$

Where L was the length of the model and U_∞ was the free-stream velocity. This is based on the requirement that an ergodic set of turbulent mean flow data be obtained over at least 200 integral length scales. As a result, data cases at 44 m/s required a minimum of 7.27s, while data at 16 m/s required 20s of sampling time at each grid point. Thus, the sample rate for the 44 m/s test cases was set to 138 Hz, while the rate for the 16 m/s test case was set to 50 Hz.

3.2.2 Running the Tunnel and Taking Data

When the required inputs had been entered into the Labview code, a pressure offset point was taken with the wind off to provide tare values for the transducers. Next, the tunnel was turned on and run up to the desired speed. A Pitot tube mounted upstream of the model in the test section monitored the dynamic pressure, which was displayed on

the tunnel control box. This allowed for precise speed control by adjusting the tunnel fan's RPM.

When the tunnel speed was set, the Labview program was initiated to begin taking data and the traverse would move the probe to the first grid point. This was always located at a bottom corner of the grid. After sampling the data, the code would automatically traverse the probe to the next point in the grid and wait three seconds for the pressure to stabilize at the new location before collecting data. The probe was always ordered to move horizontally along the grid and after completing a row, it would take a vertical step upwards to begin data collection along the next row. The code paused data collection after the completion of the first and last two rows of the grid. At these points, the tunnel was shut down and additional pressure offsets were taken with the wind off. This allowed for the calculation of an average pressure offset value for each transducer. The tunnel was then restarted and run back up to the test speed so that acquisition could continue. Depending on the size of the grid, surveys usually took between 1.5 to 2.5 hours.

3.3 Data Reduction

3.3.1 Codes Used

When testing had finished, the data taken by Labview were transferred first to the Matlab reduction code and then to the Multiprobe code that were described in Sections 2.3 and 2.5. The results from Multiprobe were the total and static pressure, the total and the three velocity component magnitudes, the total and static temperatures, density, and

rotation angles of the flow at each grid point. These data were then input into a series of Matlab drag, lift, and circulation analysis codes that produced plots of the wake velocity profile, the secondary flow profile, and the stream-wise vorticity, calculated the profile drag and induced drag, calculated the lift and circulation around vortices, and then found various force coefficients.

3.3.2 Data Rotation

In the drag analysis codes, the first thing that was done was rotating the data to correct for a slight probe misalignment with the free-stream flow. Choi and Simpson (1987) took hot wire surveys of the Stability Tunnel to find the strength of the secondary flow in the tunnel. Using these data and the secondary flow data taken by the seven-hole probe, a rotation could be performed to try and match up the two data sets. The matching was only done for the secondary flows in the free-stream portion of the wake surveys, since the secondary flow in the wake region was governed by the wake itself. Throughout the duration of the tests, the probe remained fixed in place on the sting and the same rotations were applied to each test case. The rotations were very slight in yaw and pitch, being -3° and 3.1°, respectively. This indicated that the seven-hole probe was pretty well aligned to the flow direction. Roll, however, was found to be quite far off and required a rotation of 168°. For the 0° angle of attack test cases, the secondary flows were on the order of 0.5 m/s and the rotations had virtually no impact on the axial velocity data within the level of uncertainties; they were still performed to ensure that the data were as correct as possible. However, for the 10° angle of attack test cases, the secondary flows were much more substantial, going up to 10 m/s in the two higher speed test cases, and the rotations had a more significant impact on the data.

3.3.3 Data Interpolation

After rotation, the data were interpolated onto a finer grid to have more data points to integrate and get a better drag estimate. As mentioned previously, the increment between grid points was 5.08 cm; this is too large a distance between points to obtain a very accurate drag calculation. However, due to time and data storage constraints, taking a really fine grid of data was impractical. To solve this problem, a least squares method for fitting a quadratic surface onto sample data, as described by Eberly (2001), was used. In this method, the interpolated value of data at any point on a finer grid was calculated by fitting a quadratic surface to the ten original data points that are closest to the interpolation point. Thus, the data were interpolated from a coarse 5.08 cm square grid onto a fine 0.635 cm square grid. The resulting number of total grid points was thereby increased by a factor of 64; test cases that started with 135 to 266 original data points now had 8640 to 17024 points.

Figure 3.8 and Figure 3.9 show the transformation of the wake velocity profile for Test Case #1 (44.18 m/s free-stream, 0° angle of attack, trips applied) from the initial coarse grid to the fine grid. In both figures, the wire wakes are very apparent in diagonal bands coming from the corners of the plot and running to the center. These plots are typical of the grid interpolation for every test case. In these plots, the velocity has been normalized by the mean free-stream value and the contours show the fraction (U/U_∞). The velocity indicated in the plot title represents the mean free-stream velocity and "S&L" is an abbreviation for "Straight-and-Level", as the 0° angle of attack test cases were aligned precisely with the on-coming flow.

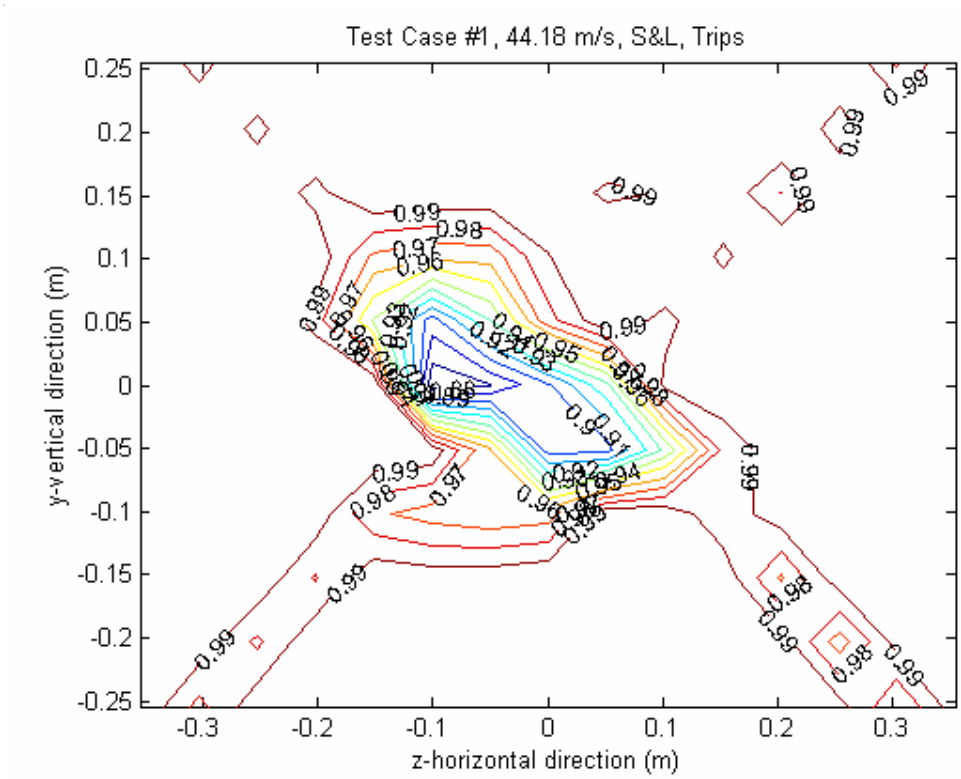

Figure 3.8: **Test Case #1, Wake Velocity Profile Using the Original Data Grid**

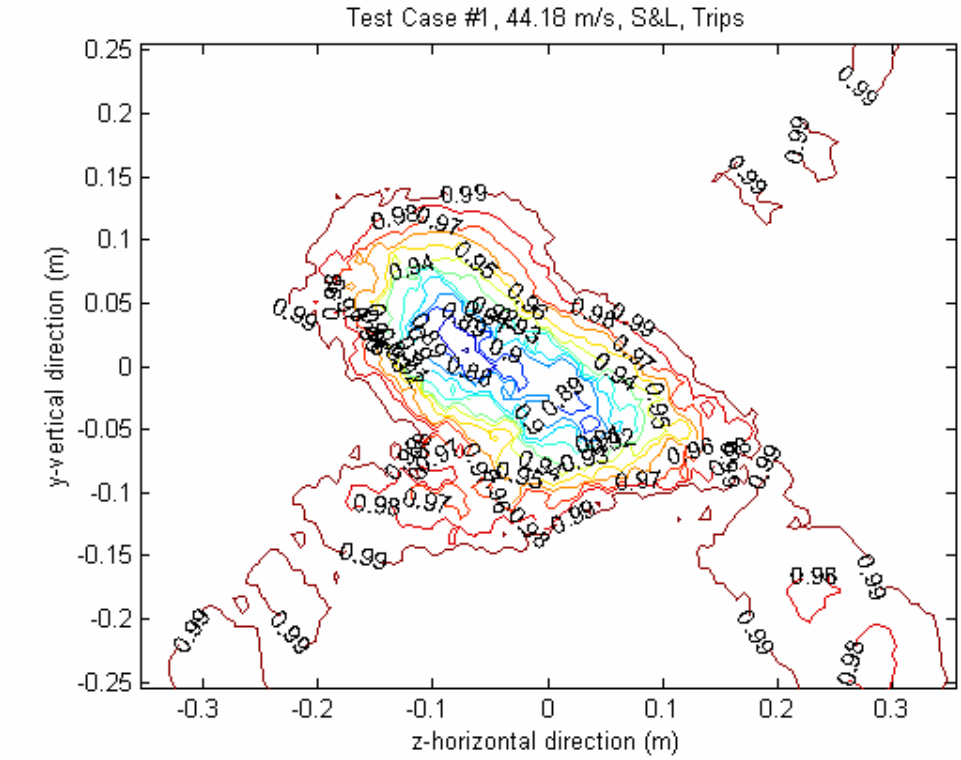

Figure 3.9: Test Case #1, Wake Velocity Profile Using a Fine Data Grid

3.3.4 Creating a Uniform Free-stream

After the data had been interpolated, the wire wakes had to be removed so that they did not interfere with the drag calculation. The data were examined closely to identify the regions of wire wake and these regions were replaced with averaged values from the surrounding free-stream data. Extreme care was taken to only remove what was perceived to be the wire wake in the free-stream portion of the grid survey, so that the wake coming from the body was not modified in any way. To see how much of an influence the wire wakes could potentially have on the drag, calculations were performed with the wakes left in the velocity profile for test case #1. The results showed that the length-squared drag coefficient (Equation 47) increased by 27%, demonstrating the importance of making sure that the wire wakes were removed.

Lastly, before a drag calculation could be performed, spatial fluctuations in the free-stream flow values were removed so that the free-stream region in the wake survey was made uniform and did not contribute to the drag. Typically, the flow speed of the free-stream regions of the wake varied by no more than 0.2 or 0.3 m/s. This was not surprising considering the very long duration of each testing period, where flow temperatures were seen to increase or decrease by 2°C to 3°C. Since the seven-hole probes' pressure and velocity measurements were not normalized by the values measured from the upstream tunnel Pitot-static probe, drift in the tunnel conditions could not be accounted for in this manner. However, since variations in the free-stream velocity were only around 0.2 to 0.3 m/s, the drift in tunnel conditions was not thought to be very severe.

To remedy this situation, average values of the free-stream speed, pressure, density, and temperature were chosen to overwrite all of the free-stream regions. This was done very carefully, so that no areas in the survey that were influenced by the model's wake were overwritten with free-stream data. Figure 3.10 shows the Test Case #1 (44.18 m/s free-stream, 0° angle of attack, trips applied) wake velocity profile after the wire wakes were removed and the free-stream areas were made uniform. Clearly, there is a significant difference in the velocity profiles between Figure 3.10 and Figure 3.9, as all the areas of velocity deficit have been removed from the free-stream leaving only what is due to the body wake. With the data now in this format, a drag calculation could be made.

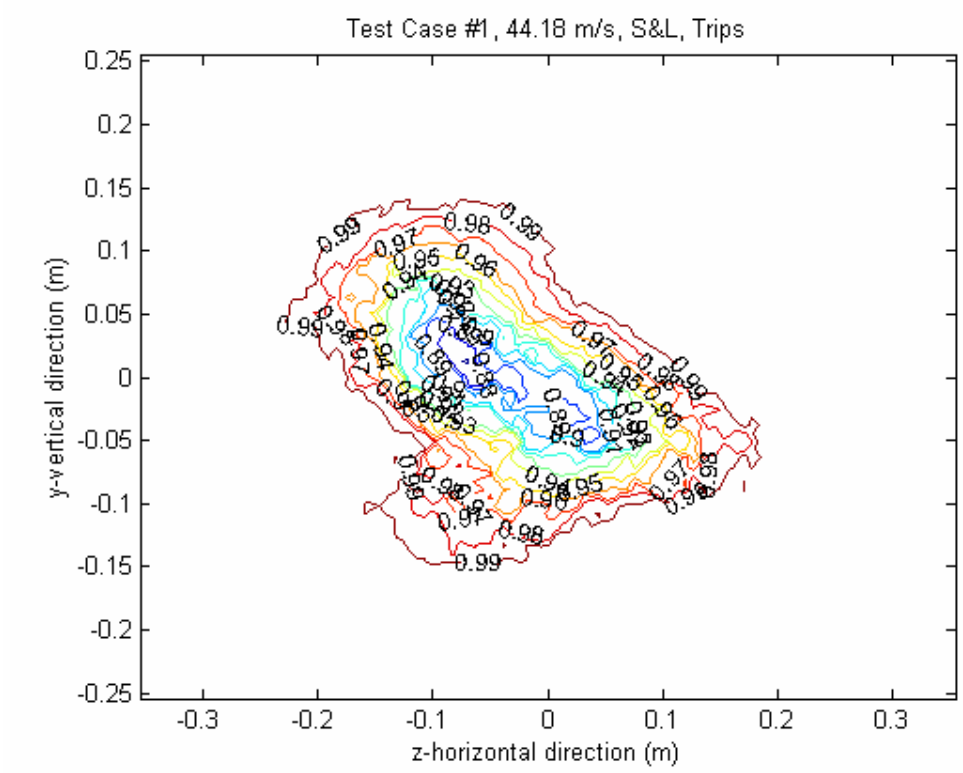

Figure 3.10: Final Wake Velocity Profile for Case #1 with No Wire Wakes and a Uniform Free-stream

3.4 Drag Calculation

3.4.1 Formulation of the Total Drag Equation

Figure 3.11 shows an idealized control volume and coordinate system around an airplane model (the ellipsoid model would work just as well) to provide a basis for the derivation of the drag equations. The two y-z planes in the control volume are denoted by S_1 and S_2, while x-z planes are denoted by S_3 and S_4, and the x-y planes are denoted by S_5 and S_6.

Several control volume and flow assumptions are made for the derivation of the drag. First, the upstream y-z plane (S_1) is assumed to be located far enough ahead of the model so that the incoming flow satisfies undisturbed free-stream conditions. Next, the wake survey data is measured only on the downstream y-z plane (S_2). The walls of the tunnel form a uniform cross-section, are parallel to the oncoming flow, and are solid surfaces with no blowing or suction allowed. Finally, the flow at the wake survey plane is steady, incompressible, and subsonic.

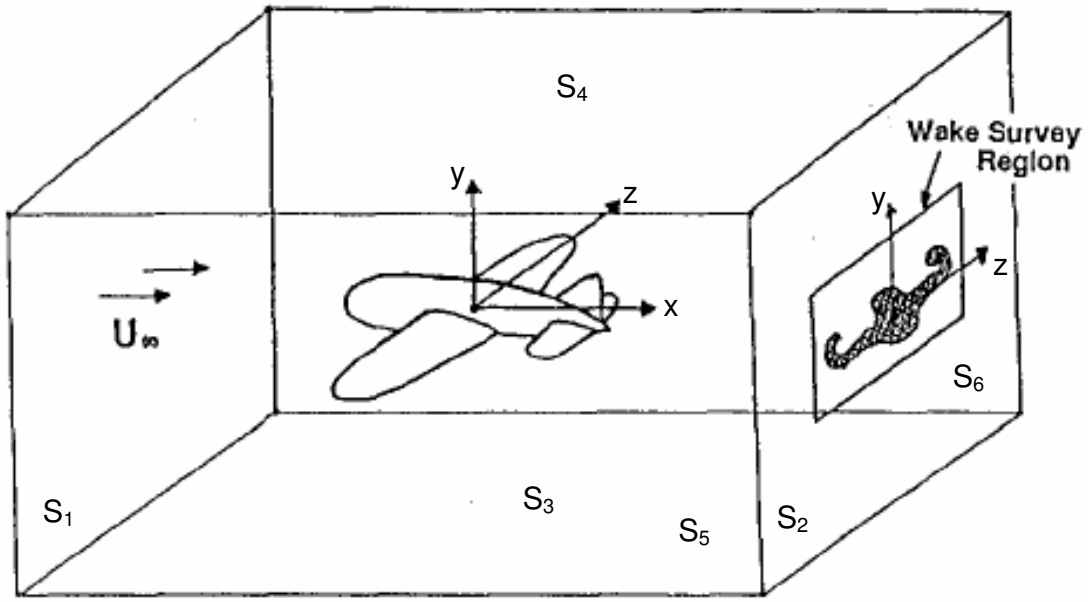

Figure 3.11: Control Volume for Derivation of Drag Equations (Adapted from Kusunose, 1997)

Neglecting any body or shear forces, the total drag (D) on the body can be determined by calculating the change of momentum in the x-direction:

$$D = \iint_{S_1} \left(P + \rho U^2\right) ds - \iint_{S_2} \left(P + \rho U^2\right) ds \tag{12}$$

where P is the static pressure, ρ is the free-stream density, and U is the axial velocity. By substituting the equation for total pressure (P_t) into Equation 12:

$$P_t = P + \frac{\rho}{2}(U^2 + V^2 + W^2) \tag{13}$$

where V and W are the secondary flow velocities and then considering that the flow in the S_1 plane satisfies the undisturbed free-stream conditions, the total drag equation can be transformed as follows:

$$D = \iint_{Wake} \left(P_{t\infty} - P_t\right) ds + \frac{\rho}{2} \iint_{S_2} \left(U_\infty^2 - U^2\right) ds + \frac{\rho}{2} \iint_{S_2} \left(V^2 + W^2\right) ds \tag{14}$$

where $P_{t\infty}$ is the free-stream total pressure and U_∞ is the free-stream velocity. The next section (3.4.2) explains how Equation 14 is divided into the profile and induced drag using velocity terms that were first introduced by Betz (1925).

3.4.2 Formulation of the Profile Drag Equation

For this study, drag calculations were performed by utilizing Betz's integral momentum method that is illustrated by Brune (1994) in experiments that are very similar to this one. In this method, an artificial axial velocity (U^*) and a perturbation velocity (U') are introduced:

$$U^* = \sqrt{U^2 + \frac{2(P_{t\infty} - P_t)}{\rho}} \tag{15}$$

$$U' = U^* - U_\infty \tag{16}$$

Using these definitions and knowing that $U^* = U$ outside of the wake, the second integral in Equation 14 can be rewritten as follows:

$$\iint_{S_2} \left(U_\infty^2 - U^2\right) ds = \iint_{S_2} \left(U_\infty^2 - U^{*2}\right) ds + \iint_{Wake} \left(U^{*2} - U^2\right) ds \tag{17}$$

By utilizing:

$$\iint_{Wake} \left(U^* - U\right) ds = -\iint_{S_2} \left(U_\infty - U^*\right) ds \tag{18}$$

the first integral on the left hand side of Equation 17 is expanded as follows:

$$\iint_{S_2} \left(U_\infty^2 - U^{*2}\right) ds = -2U_\infty \iint_{Wake} \left(U^* - U\right) ds - \iint_{S_2} \left(U^* - U_\infty\right)^2 ds \tag{19}$$

Now, by substituting Equation 19 into Equation 17, the following results after some simplification:

$$\iint_{S_2}\left(U_\infty^2 - U^2\right)ds = \iint_{Wake}\left(U^* - U\right)\left(U^* + U - 2U_\infty\right)ds - \iint_{S_2} U'^2\, ds \tag{20}$$

By substituting Equation 20 into Equation 14, the total drag is now expressed as follows:

$$D = \iint_{Wake}\left[P_{t\infty} - P_t + \frac{\rho_\infty (U^* - U)(U^* + U - 2U_\infty)}{2}\right]ds + \frac{\rho}{2}\iint_{S_2}\left(V^2 + W^2 - U'^2\right)ds \tag{21}$$

At this point, Maskell (1972) introduces a uniform blockage velocity (U_b):

$$U_b = \frac{1}{2A}\iint_{Wake}\left(U^* - U\right)ds \tag{22}$$

where A is the cross-sectional area of the tunnel. With U_b, the U'^2 term in the second integral of Equation 21 is re-expressed as:

$$\frac{\rho}{2}\iint_{S_2} U'^2 ds = \rho U_b \iint_{Wake}\left(U^* - U\right)ds \tag{23}$$

Substituting Equation 23 into Equation 21 yields the final expression of the total drag:

$$D = \iint_{Wake}\left[P_{t\infty} - P_t + \frac{\rho_\infty \left\{U^* - U\right\}\left\{U^* + U - 2\left(U_\infty + U_b\right)\right\}}{2}\right]ds + \frac{\rho}{2}\iint_{S_2}\left(V^2 + W^2\right)ds \tag{24}$$

With the total drag in this form, it is easy to break the equation into the profile (D_p) and induced (D_i) drag components:

$$D_p = \iint_{Wake}\left[P_{t\infty} - P_t + \frac{\rho_\infty \left\{U^* - U\right\}\left\{U^* + U - 2\left(U_\infty + U_b\right)\right\}}{2}\right]ds \tag{25}$$

$$D_i = \frac{\rho}{2}\iint_{S_2}\left(V^2 + W^2\right)ds \tag{26}$$

For this study, it was found that U_b was negligibly small for all of the test cases and could be left out of the final profile drag equation, which can be solved entirely by data collected in the wake region:

$$D_p = \iint_{Wake} \left[P_{t\infty} - P_t + \frac{\rho_\infty (U^* - U)(U^* + U - 2U_\infty)}{2} \right] ds \qquad (27)$$

3.4.3 Formulation of the Induced Drag Equation

From the previous section, the induced drag is defined by Equation 26. However, this equation can not be utilized in this study, since data were obtained in the wake region only. To get around this problem, Maskell (1972) introduces several equations to transform Equation 26 so that it can be solved by using data from the wake region only.

Maskell (1972) first defines the axial component of the vorticity (ξ) and the cross-flow divergence (σ):

$$\xi = \frac{\partial V}{\partial z} - \frac{\partial W}{\partial y} \qquad (28)$$

$$\sigma = \frac{\partial V}{\partial y} + \frac{\partial W}{\partial z} = \frac{-\partial U}{\partial x} \qquad (29)$$

Then a stream function (Ψ) and a velocity potential (Φ) are calculated by solving the Poisson equation:

$$\frac{\partial^2 \Psi}{\partial y^2} + \frac{\partial^2 \Psi}{\partial z^2} = -\xi \qquad (30)$$

$$\frac{\partial^2 \Phi}{\partial y^2} + \frac{\partial^2 \Phi}{\partial z^2} = \sigma \qquad (31)$$

Boundary conditions for Equation 30 must satisfy $\Psi = 0$ along the edges of the tunnel walls. For Equation 31, a $\frac{\partial \Phi}{\partial n} = 0$ boundary condition is enforced on the edges of the tunnel walls. Finally, to satisfy Equations 28 and 29, Maskell (1972) expresses the *V* and *W* velocities as follows:

$$V = \frac{\partial \Phi}{\partial y} - \frac{\partial \Psi}{\partial z} \tag{32}$$

$$W = \frac{\partial \Phi}{\partial z} + \frac{\partial \Psi}{\partial y} \tag{33}$$

With Equations 28 through 33, the induced drag from Equation 26 can be transformed as follows, according to Wu (1979):

$$D_i = \frac{\rho}{2}\left[\iint_{S_2}\left(\frac{\partial}{\partial y}(\Psi W) - \frac{\partial}{\partial z}(\Psi V)\right)ds + \iint_{S_2}\left(\frac{\partial}{\partial y}(\Phi V) + \frac{\partial}{\partial z}(\Phi W)\right)ds + \iint_{S_2}(\Psi\xi - \Phi\sigma)ds\right] \tag{34}$$

Taking advantage of Stokes' theorem for the first integral and the divergence theorem for the second integral, Equation 34 can be rewritten as follows:

$$D_i = \frac{\rho}{2}\left[\oint_b (\Psi U_t)dl + \oint_b (\Phi U_n)dl + \iint_{S_2}(\Psi\xi - \Phi\sigma)ds\right] \tag{35}$$

where b is the boundary of S_2 on the tunnel walls and U_t and U_n are the tangential and normal components of the velocity vector. Since Ψ and U_n are zero on b and the contribution of the third integral is negligibly small outside of the wake region, the final form of the induced drag equation can be approximated as:

$$D_i \approx \frac{\rho}{2}\iint_{Wake}[\Psi\xi - \Phi\sigma]ds \tag{36}$$

3.4.4 Numerical Integration to Obtain the Drag

In the data analysis code, the integration of the profile drag in Equation (27) was handled by implementing a composite trapezoidal numerical integration scheme over the entire two-dimensional domain of the wake survey region. Next, ξ and σ (Equations 28

and 29) were found by approximating the partial derivatives of V and W. For instance, $\frac{\partial W}{\partial y}$ was found by the following equation:

$$\left.\frac{\partial W}{\partial y}\right|_i = \frac{W_{i+1} - W_{i-1}}{y_{i+1} - y_{i-1}} \tag{37}$$

The other partial derivatives were found by similar equations.

With ξ and σ, Ψ and Φ (Equations 30 and 31) were found by solving Poisson's equation using the Gauss-Siedel iterative method. In this method, iterative guesses at the solution were made until the averaged L_2 norm of the residue was less than 10^{-8}. When Ψ and Φ had been obtained, the induced drag (Equation 36) could be calculated. This was again handled by implementing a composite trapezoidal numerical integration scheme over the entire two-dimensional domain of the wake survey region. The total drag was then found by adding the profile and induced drag. Finally, drag coefficients normalized by length squared, frontal area, and wetted area were found so that the drag between different test cases could be compared.

3.5 Circulation and Lift Calculation

3.5.1 Formulation of the Circulation Equation

In addition to the induced drag calculation, the axial component of the vorticity could be used to find the circulation of the vortices being shed from the model in the wake survey plane. Stokes' theorem gives the following equation for the circulation (Γ) around a surface bounded by a closed curve:

$$\Gamma = \iint_S \left[\vec{\Omega} \bullet \vec{n}\right] ds \tag{38}$$

where $\vec{\Omega}$ is the vorticity vector and $\vec{n}$ is the surfaces' normal vector. For the y-z wake survey plane, $\vec{n}$ is aligned along the x-axis and $\vec{\Omega} \bullet \vec{n}$ becomes ξ, the axial component of the vorticity. Thus, Equation 38 can be re-written to find the circulation in the wake survey plane:

$$\Gamma = \iint_{Wake} [\xi] ds \tag{39}$$

3.5.2 Formulation of the Lift Equation

By applying the integral momentum equation in the vertical direction for the control volume shown in Figure 3.11 and assuming the same flow conditions as the drag calculation, the following equation gives the lift on the body:

$$Lift = -\iint_S \left[Pn_y + \rho V(\vec{U} \bullet \vec{n})\right] ds \tag{40}$$

where $\vec{U}$ is the velocity vector. Expanding this equation over the faces of the control volume yields:

$$Lift = \rho \iint_{S_{1,2}} [(UV)_1 - (UV)_2] ds + \iint_{S_{3,4}} \left[\left(P + \rho V^2\right)_3 - \left(P + \rho V^2\right)_4\right] ds + \rho \iint_{S_{5,6}} [(WV)_5 - (WV)_6] ds \tag{41}$$

If Equation 13 is substituted into Equation 41, the perturbation velocities: $u = U - U_\infty$, v = V, $w = W$ are introduced, and the contribution of the square of perturbation velocities (v^2, w^2) outside of S_2 are neglected, the lift equation, after some simplification, becomes:

$$Lift = \rho \iint_{S_{1,2}} \left[(U_\infty v)_1 - (U_\infty v)_2 - (uv)_2\right] ds + \rho \iint_{S_{3,4}} \left[(U_\infty u)_4 - (U_\infty u)_3\right] ds \tag{42}$$

Further simplification leads to the following equation:

$$Lift = \rho U_\infty \left(\iint_{S_{1,2}} [v_1 - v_2] ds + \iint_{S_{3,4}} [u_4 - u_3] ds \right) + \rho \iint_{S_2} [v(U_\infty - U)] ds \tag{43}$$

At this point, Van Dam (1991) introduces the span-wise circulation and integration by parts, so that Equation 43 becomes:

$$Lift = \rho U_\infty \iint_{S_2} [z\xi] ds + \rho \iint_{S_2} [v(U_\infty - U)] ds \tag{44}$$

The first integral in Equation 44 is expressed in terms of the axial component of the vorticity, which vanishes outside the viscous wake. Thus, it only requires measurements in the wake. The second integral in Equation 44 is negligible in the free-stream and very small inside of the wake when the difference between the free-stream and axial velocity is multiplied by the vertical velocity. Thus, it can be normally be neglected so that the lift can be approximated by:

$$Lift \approx \rho U_\infty \iint_{Wake} [z\xi] ds \tag{45}$$

3.5.3 Numerical Integration to obtain the Circulation and Lift

Like with the drag calculations in the data analysis code, the integration of the circulation (Equation 39) and the lift (Equation 45) was handled by implementing the composite trapezoidal numerical integration scheme over the appropriate area in the wake survey plane. Circulation was calculated around each vortex that was seen in the wake survey region for test cases 3 through 5. This required that the integration region be split along the vertical line at $z = 0$ to separate the two vortices that were formed. The entire wake survey region was used in the calculation of the lift. This concluded the extent of the data analysis in this study. Uncertainty in the results is discussed in Chapter 4.

4 Results and Discussion

4.1 Wake Profiles

Following the procedure outlined by Chapter 3, the drag was calculated for all five of the test cases. Figures 4.1 through 4.5 show the final wake velocity profiles of all of the test cases after the wire wakes had been removed and the free-stream regions had been made uniform. All profiles were taken one model length downstream of the ellipsoid's trailing edge. All velocities have been normalized by the mean free-stream value and the contours show the fraction (U/U_∞).

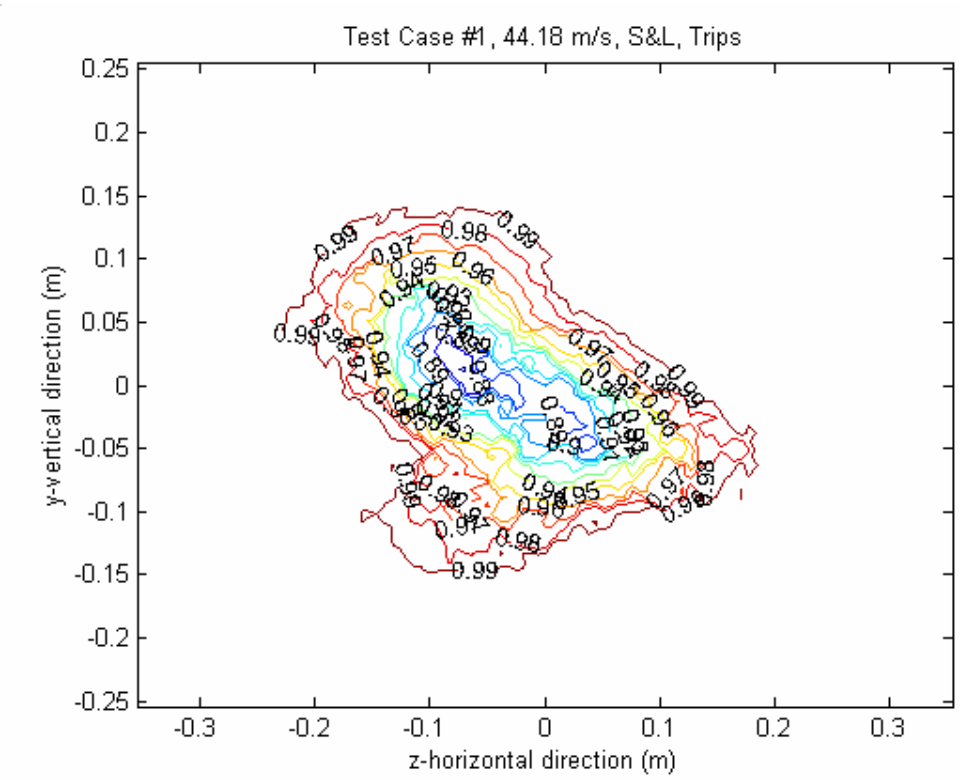

Figure 4.1: Wake Profile for Test Case #1 (44.18 m/s free-stream, 0° AOA, trips applied)

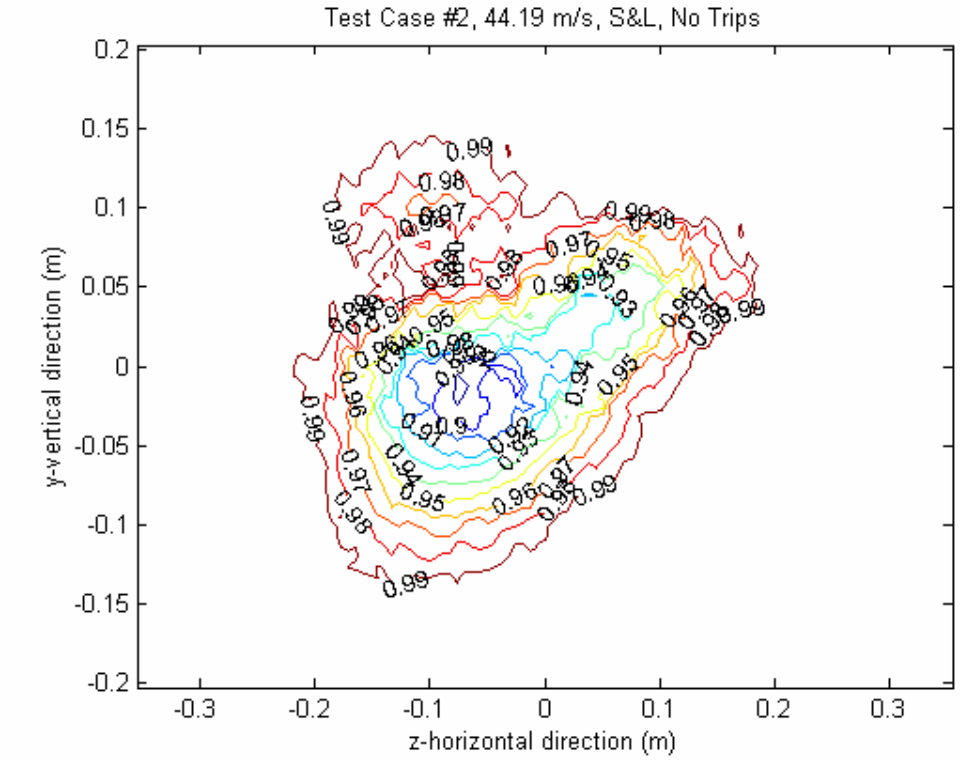

Figure 4.2: Wake Profile for Test Case #2 (44.19 m/s free-stream, 0° AOA, no trips)

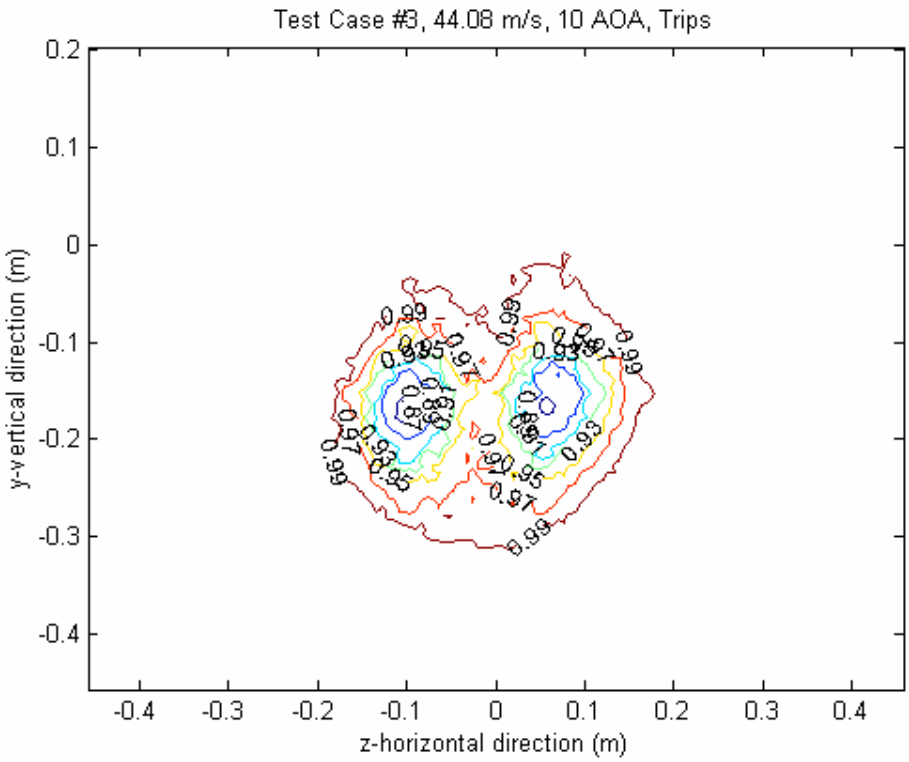

Figure 4.3: Wake Profile for Test Case #3 (44.08 m/s free-stream, 10° AOA, trips applied)

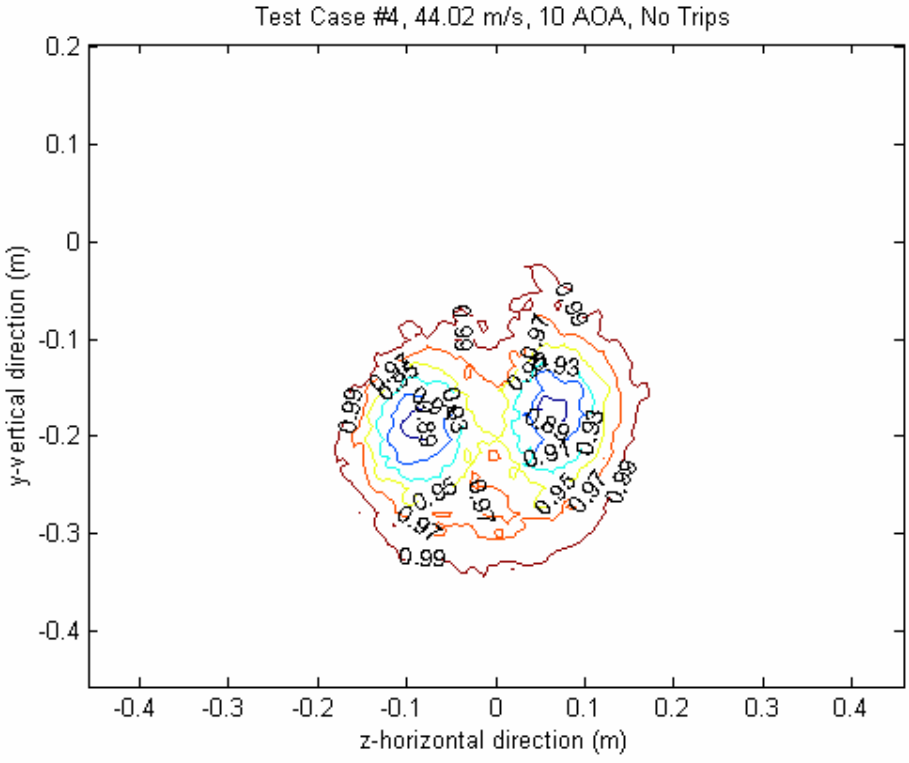

Figure 4.4: Wake Profile for Test Case #4 (44.02 m/s free-stream, 10° AOA, no trips)

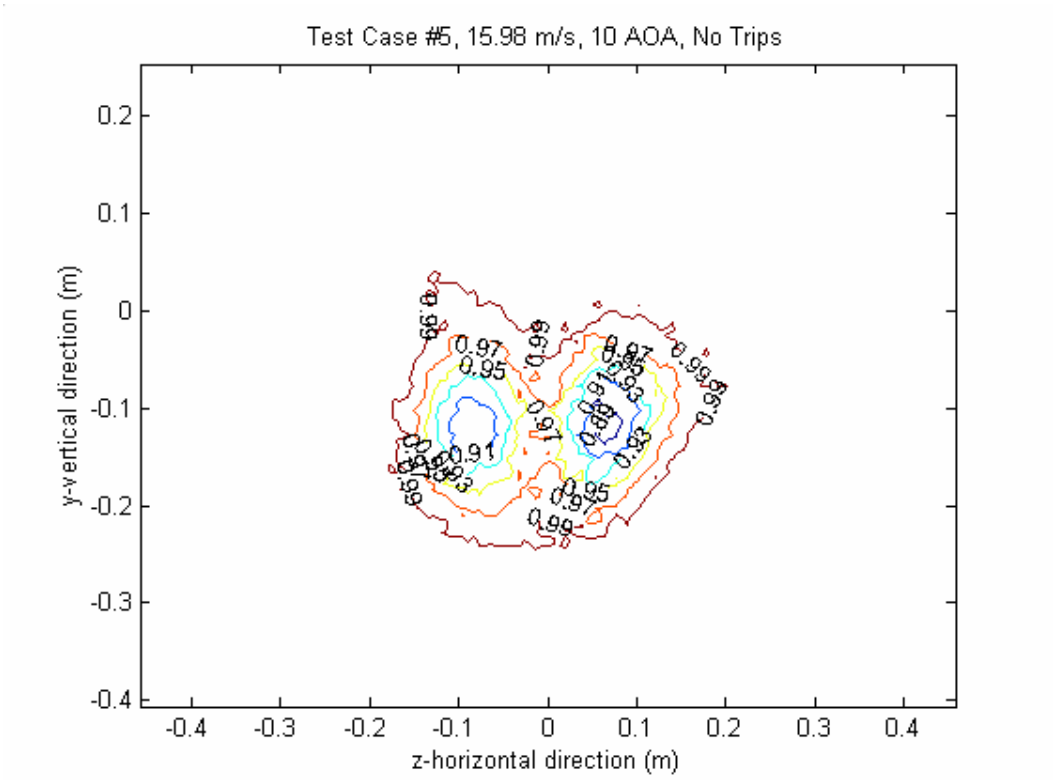

Figure 4.5: Wake Profile for Test Case #5 (15.98 m/s free-stream, 10° AOA, no trips)

4.1.1 Differences in the Wake Due to Angle of Attack

In examining the five plots, a striking difference is observed between the two 0° angle of attack cases and the three 10° angle of attack cases. The 0° cases appear to be made up of only a single, wide velocity deficit region while the 10° cases are made up of two circular vortices. The reason for this is that the symmetric model, when aligned straight-and-level with the flow, has an equal pressure distribution on the top and bottom surfaces, producing no lift or induced drag and should not produce vortices. When aligned at a 10° angle of attack, the flow over the upper surface of the model is accelerated creating a lower pressure than that on the bottom surface of the model. As a by-product of this pressure differential, lift, induced drag, and a pair of counter-rotating trailing vortices are created.

4.1.2 Differences in the Wake between the Straight-and-Level Cases

Looking at Figures 4.1 and 4.2, there are some strange differences between the two straight-and-level test case wake profiles. The only difference in the flow conditions between the test cases is that case #1 (Figure 4.1) has trip strips applied to the leading edge, while test case #2 (Figure 4.2) does not have any trips. Yet, the wake of case #1 appears to be aligned diagonally, running from the northwest to the southeast of the plot domain, while the wake of case #2 appears to run diagonally from the southwest to the northeast of the plot domain. Additionally, case #2 has a small velocity deficit region around grid coordinate (-0.1, 0.1).

There is no clear explanation as to why the two wake profiles look this way. Since the symmetric model is aligned straight-and-level with the flow with no yaw or roll angle, it would be reasonable to expect that the wake would be aligned horizontally across the domain instead of diagonally. This was what had been observed in the NNEMO wake profiles. Also, the addition and subtraction of the trips does not really explain why the wake shifts its diagonal alignment between the two test cases. It is not believed that irregularities in the way the trips were setup on the model or that any sticky residue left over on the model surface when the trips were removed could have caused the differences seen in the wake profiles. The data indicated that the secondary flows in the two wakes are virtually negligible being less than 0.5 m/s. Also, the rotations of the data had no noticeable effect on the appearance of the wake profiles. Finally, the wire wakes in both cases were removed (notice the difference between Figures 3.8 and 4.1) and don't appear to have any effect on the remaining velocity profile.

4.1.3 Differences in the Wake between the 10° Angle of Attack Cases

The wake profiles in the other three test cases are very similar to each other and appear as would be expected. In all of the cases, the centers of the two counter-rotating vortices are aligned horizontally with each other and are pretty symmetric. There is not much of a difference in the wake profiles between test cases 3 (Figure 4.3) and 4 (Figure 4.4), where the only changes in the flow conditions were the addition and subtraction of trip strips. However, the velocity deficit in test case #3 is slightly greater than that of case #4, indicating a higher drag. Test case #5 (Figure 4.5) differs from the other two test cases only in that the flow speeds are much less, being around 16 m/s compared to 44 m/s. The basic form of case #5's wake profile remains the same as that seen in cases #3 and #4.

4.2 Secondary Flow Velocity Profiles

In addition to the wake velocity profile figures, plots of the secondary flow (*V* and *W*) were produced to show the direction of the counter-rotating vortices coming off the model at a 10° angle of attack (Figures 4.6 to 4.8). All profiles were taken one model length downstream of the ellipsoid's trailing edge. Since the $\frac{V}{U_\infty}$ and $\frac{W}{U_\infty}$ ratios were less than 0.01 and there was no clear structural organization in the 0° angle of attack test cases, their secondary velocity plots are not shown.

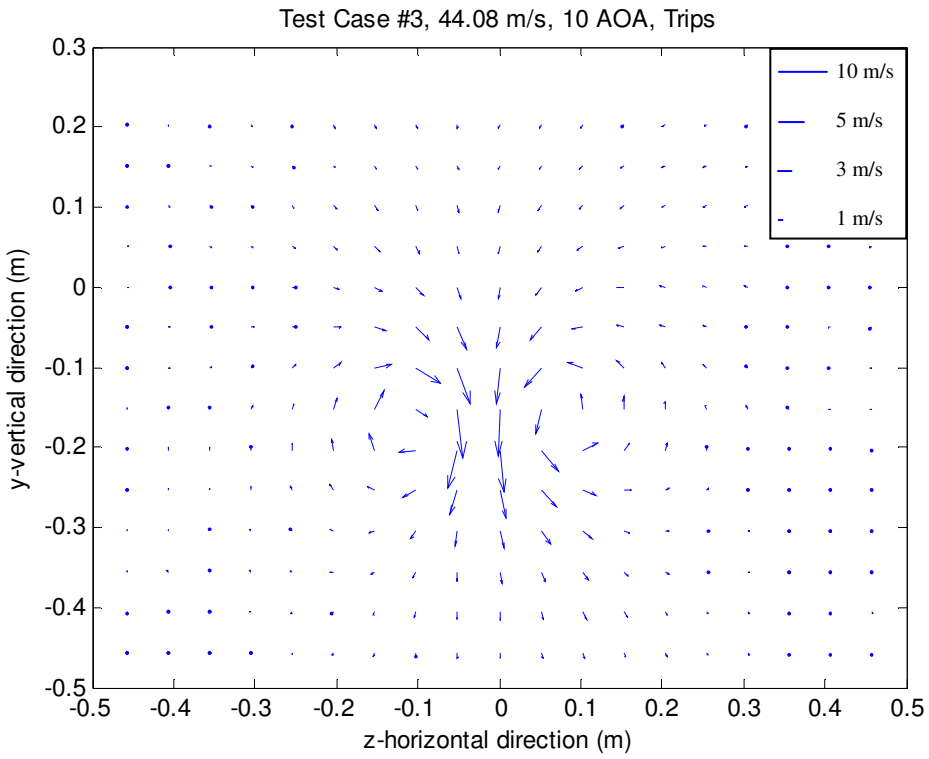

Figure 4.6: Secondary Flow Profile for Test Case #3 (44.08 m/s free-stream, 10° AOA, trips applied)

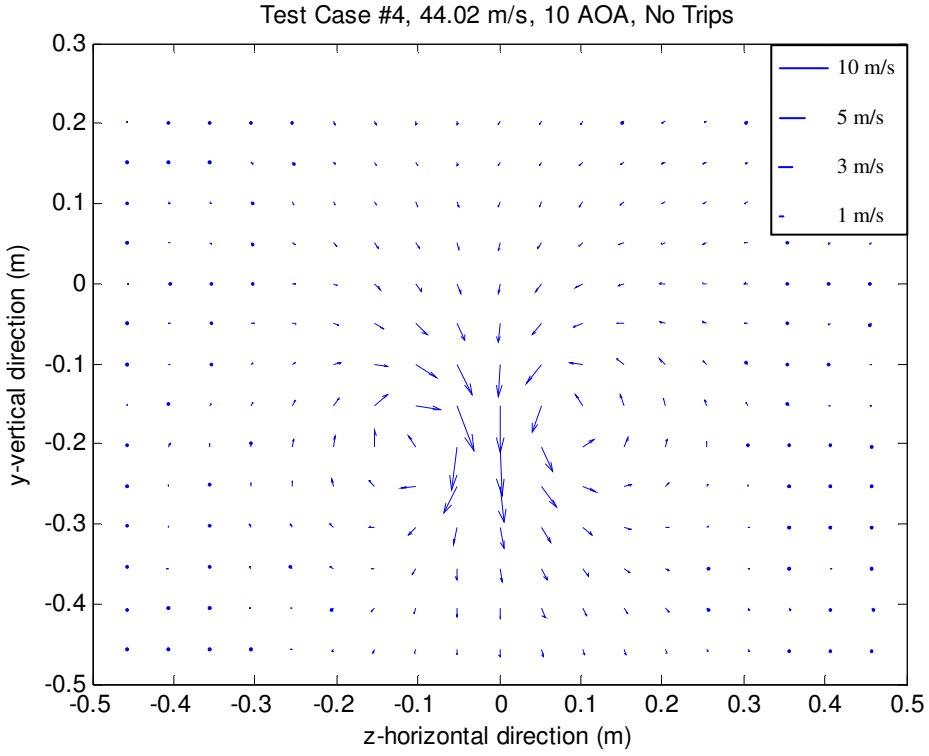

Figure 4.7: Secondary Flow Profile for Test Case #4 (44.02 m/s free-stream, 10° AOA, no trips)

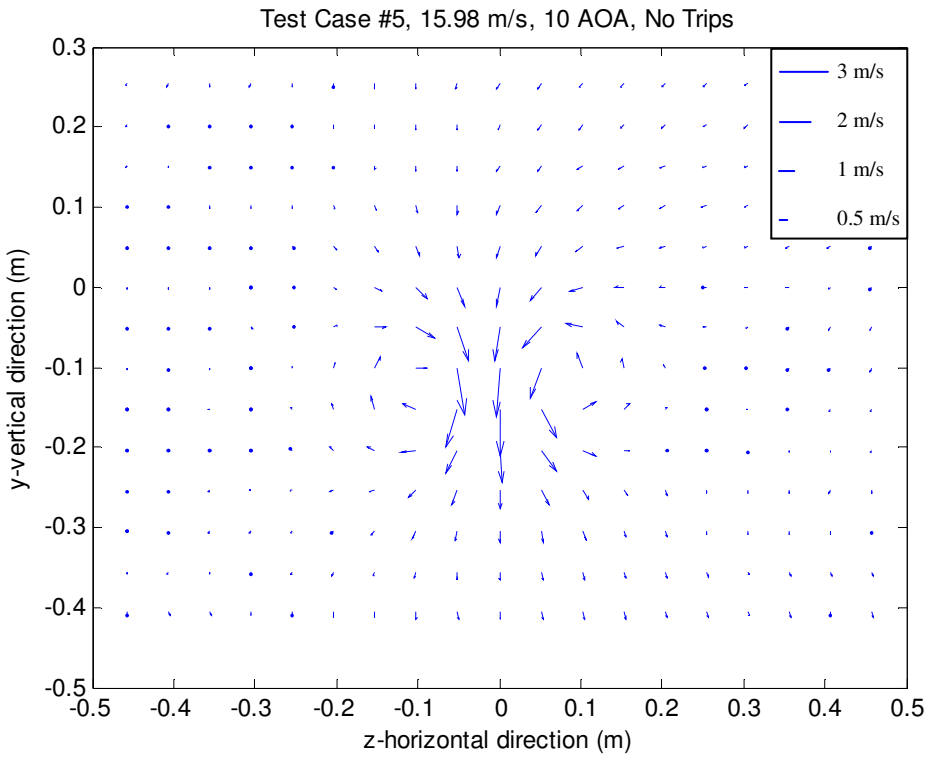

Figure 4.8: Secondary Flow Profile for Test Case #5 (15.98 m/s free-stream, 10° AOA, no trips)

4.2.1 Description of the Secondary Flows

There is virtually no difference in the appearance of the secondary flows between test cases 3 to 5. However, the magnitude of the velocities in test cases #3 and #4, which were high speed cases, is generally in the 5 m/s to 10 m/s range in the region of the wake centerline. Test case #5, the low speed case, has velocities of 1 m/s to 3 m/s in this region. For all cases, the left vortex rotates clockwise while the right vortex rotates counter-clockwise, producing a region of downwash in-between the two. Outside of the region of strong vortical flow, the free-stream values of the secondary velocities are very small and practically negligible in their contribution to the induced drag.

4.2.2 Influence of the Secondary Flows on the Wake Profiles

It is interesting to note that the centers of rotation and the relative region of strong vortical flow in Figures 4.6 – 4.8 coincide with the lowest speed areas of the wake and the relative size of the wake seen in Figures 4.3 – 4.5, respectively. This indicates that the counter-rotating vortices are the main driving factor in the characteristics of the wake. For instance in Figure 4.6, the centers of the two vortices are located at approximately (-0.13, -0.18) and (0.08, -0.18); this corresponds with the lowest speed regions seen in Figure 4.3. In Figure 4.6, the size of the region of strong vortical flow extends roughly between -0.25 m to 0.2 m in the z-direction and between -0.35 m to 0 m in the y-direction. This also approximately defines the wake deficit region shown by Figure 4.3. Table 4.1 presents the centers of the vortices in Figures 4.6 – 4.8 and also gives the approximate size of the wake region.

Test Case and Figure Number	Vortex Centers (m)	Wake Region (m)
Test Case #3, Figure 4.6	(-0.13, -0.18) (0.08, -0.18)	z: -0.25 to 0.20 y: -0.35 to 0.00
Test Case #4, Figure 4.7	(-0.13, -0.18) (0.08, -0.18)	z: -0.25 to 0.20 y: -0.35 to 0.00
Test Case #5, Figure 4.8	(-0.13, -0.13) (0.08, -0.13)	z: -0.25 to 0.20 y: -0.30 to 0.05

Table 4.1: Centers and Sizes of the Vortical Regions in Test Cases 3-5

4.2.3 Effect of the Downwash on the Wake Profiles

One important thing to note about the data in Table 4.1 is that the vortex centers and wake region size are identical for the two high speed test cases (#3 and #4). This was to be expected since the model positioning and test conditions were practically the same, except that the trip strips were removed from the model in test case #4. It is also notable that the center of the wake for these two test cases is positioned lower (at y = -0.18 m)

than the wake deficit centers seen in test cases #1 and #2, which were positioned close to y = 0 m. This is due to the downwash created from the counter-rotating vortices in test cases #3 and #4. Since test cases #1 and #2 have no counter-rotating vortices and downwash, their wakes do not move towards the tunnel floor like they do in test cases #3 and #4.

Taking this into account, the low speed test case (#5) has vortex centers and a wake region that is centered at y = -0.13 m, which is 0.05 m higher than the high speed cases. This means that the wake for test case #5 moved downwards in the tunnel at a smaller angle compared to test cases #3 and #4. This was an unexpected result as it was thought that the wake would traverse downwards at the same angle and be positioned at the same place in the wake survey region for the three angle of attack test cases. However, the V/U_∞ ratio for the high speed test cases was slightly higher (0.23) than the V/U_∞ ratio for the low speed test case (0.19) accounting for the difference. This difference may be due to Reynolds number effects on the formation and separation of the counter-rotating vortices on the model.

4.3 Drag Results

Table 4.2 summarizes all of the drag calculations for the five test cases. Please note that the following abbreviations were used to save space: (D_p) profile drag, (D_i) induced drag, (D) total drag, (C_D) drag coefficient, (C_{DL}) length-squared drag coefficient, (C_{DF}) frontal area drag coefficient, (C_{DW}) wetted area drag coefficient, (U_∞) free-stream velocity, and (Re_L) length-based Reynolds number.

The length-based Reynolds number was defined as follows:

$$\mathrm{Re}_L = \frac{U_\infty L}{\nu_\infty} \tag{46}$$

where ν_∞ is the free-stream kinematic viscosity and L is the model length (1.6 m). The length-squared drag coefficient was then calculated from:

$$C_{DL} = \frac{D}{0.5\rho U_\infty^2 L^2} \tag{47}$$

The frontal area drag coefficient was found from:

$$C_{DF} = \frac{D}{0.5\rho U_\infty^2 FA} \tag{48}$$

where FA is the frontal area of the model (0.0726 m^2). Finally, the wetted area drag coefficient was calculated using:

$$C_{DW} = \frac{D}{0.5\rho U_\infty^2 WA} \tag{49}$$

where WA is the wetted area of the model (1.487 m^2).

Test Case	Drag (N)	C_D	U_∞ (m/s)	Re_L
#1: 44 m/s, 0° AOA, Trips	D_p = 7.01 D_i = 0 D = 7.01	C_{DL} = 0.0026 C_{DF} = 0.0921 C_{DW} = 0.0045	44.18	4.3 x 10^6
#2: 44 m/s, 0° AOA, No Trips	D_p = 6.51 D_i = 0 D = 6.51	C_{DL} = 0.0024 C_{DF} = 0.0852 C_{DW} = 0.0042	44.19	4.3 x 10^6
#3: 44 m/s, 10° AOA, Trips	D_p = 8.34 D_i = 1.13 D = 9.47	C_{DL} = 0.0035 C_{DF} = 0.1221 C_{DW} = 0.0060	44.08	4.3 x 10^6
#4: 44 m/s, 10° AOA, No Trips	D_p = 7.71 D_i = 0.996 D = 8.71	C_{DL} = 0.0032 C_{DF} = 0.1119 C_{DW} = 0.0055	44.02	4.3 x 10^6
#5: 16 m/s, 10° AOA, No Trips	D_p = 0.785 D_i = 0.081 D = 0.866	C_{DL} = 0.0023 C_{DF} = 0.0821 C_{DW} = 0.0040	15.98	1.6 x 10^6

Table 4.2: Summary of Drag Results

4.3.1 Comparison of the Drag between the Test Cases

In examining Table 4.2, it is clear that mounting the model at a 10° angle of attack dramatically increases the drag coefficient; by comparing test case #1 to #3 and case #2 to #4, the length-squared drag coefficient increases by 33% to 35%. This is due to the addition of induced drag and an increase in the model's frontal profile with respect to the oncoming flow.

The addition of trip strips to the model appears to slightly increase the drag coefficient; for the length-squared coefficients this increase was on the order of 0.0003. The same small increase was also seen on tests from the NNEMO model adding to the evidence that this is a real effect. The reason for this may be due to a slight increase in frontal area and a roughening of the model surface. However, uncertainties in the data, discussed in Section 4.4, are high enough that the increase in drag coefficient due to the trips may be insignificant. It was also seen that uncertainty in the NNEMO tests was greater than the increase in the drag coefficients due to the trip strips.

One final thing to note is that the low speed test case (#5) produced far lower drag coefficients than the two high speed 10° angle of attack cases. This result differs from the NNEMO tests, where the lower speed flow cases had higher drag coefficients than the comparable higher speed flow cases. An explanation for this is that the critical Reynolds number on the model may be around 10^5 like what was seen in Figure 1.2, while the critical Reynolds number for the NNEMO model may have been higher. Thus, the drag coefficient may reach a minimum at a Reynolds number of 1.6 million before rising up again at higher Reynolds numbers. Because only two different Reynolds numbers were tested, more test cases at different Reynolds numbers would be needed to confirm this

hypothesis. However, overriding this analysis are the very high uncertainties attributed to the low speed case (see Section 4.4) that may render it irrelevant and not worthy of comparison with the other test cases.

In summary, the combination of angle of attack and trip strips made test case #3 the highest drag producer with a length-squared drag coefficient of 0.0035. Removing the trip strips, but keeping the angle of attack, made test case #4 the second highest drag producer with a length-squared drag coefficient of 0.0033. Next, the two straight-and-level test cases come in with test case #1 having a coefficient of 0.0026 and test case #2 having a coefficient of 0.0024. Finally, the low speed test case #5 had the smallest drag coefficient of 0.0023.

4.3.2 Comparison of the Drag with other Experiments

Due to confidentiality issues, the drag from the NNEMO study cannot be explicitly reported here. However, the results from that test do not really contradict any of the results from this test, except that the lower speed case in this study produced a lower drag coefficient than the higher speed cases as discussed in Section 4.3.1. Again, this may not really be an issue since the critical Reynolds number for the ellipsoid and the NNEMO may be different and due to the fact the uncertainty for the lower speed case is high enough that the drag coefficient may not be precisely known.

Comparing the straight-and-level results to Figure 1.2 and what was predicted in the Introduction, the drag seems very reasonable. The wetted drag coefficient for test cases #1 and #2 was 0.0045 and 0.0042, respectively. This falls into the 0.002 to 0.006 range of what was estimated in the Introduction by looking at bodies of revolution with fineness ratios between 4 and 6.93. Thus, if the drag calculations in this study are not

precise, they are a least in the right range when compared to data from previous experiments.

4.4 Uncertainty in the Drag

4.4.1 Sources of the Uncertainties

Uncertainties in the drag calculations are derived primarily from human judgment in how the free-stream data are modified to ensure uniform conditions. The raw free-stream data values fluctuated on the order of 0.2 to 0.3 m/s throughout the survey domain for each test case. To ensure that the free-stream did not contribute to the overall drag calculation, the free-stream region was made uniform by designating an average value of the velocity, pressure, density, and temperature. While these values seemed very reasonable for each test case, the true values of the free-stream data are debatable. Since small changes in the average values have a large impact on the drag calculation (see Section 4.4.2), the uncertainty in the calculation is dominated by the choice of these values.

Pisterman (2004) reports that the velocity measurements from the probe have minimal uncertainties around 1% to 2%; thus, they can probably be neglected from the overall uncertainty in the test results. Other uncertainties in the data reduction process, such as the interpolation and the numerical integration are very difficult to quantify. However, they probably contribute far less to the overall uncertainty than the uniformity modification to the free-stream data. Wire wake removal could also cause some uncertainty if it were done incorrectly, but the regions affected by the wire wake were

very obvious and were replaced using the surrounding free-stream data before the free-stream uniformity changes were even made. Thus, any additional uncertainties due to the wire wake removal are probably negated by the free-stream uniformity modification.

Taking all of this into consideration, uncertainty in the results changes on a case by case basis, largely depending on the amount of spatial fluctuation in the free-stream velocity and the corresponding total pressure. High speed flows will have lower uncertainties than the low speed flow because the spatial fluctuations of the free-stream velocity make up a smaller percent of the mean free-stream velocity value and thus have less of an effect on the data.

4.4.2 Calculation of the Uncertainty

As described in the data reduction section, average values of the free-stream data were chosen to represent the entire free-stream region for each data case. This made the free-stream region uniform so that it would not contribute to the drag calculation. While the fluctuations in the free-stream velocity values were no greater in magnitude than 0.2 to 0.3 m/s from the mean, they had a large impact on the uncertainty of the drag calculation. If small additions or subtractions are made to the mean free-stream velocity and total pressure, the drag will significantly change. To demonstrate this, calculations were performed with the mean free-stream velocity set 0.25 m/s higher and lower with a corresponding change to the free-stream total pressure to see the effect on the drag. The results are tabulated in Table 4.3. The table displays the three different speeds (0.25 m/s below the mean, the mean, and 0.25 m/s above the mean) that were used to calculate the drag, the length-squared drag coefficient calculated, and the percent difference in the drag coefficient from the mean for each test case.

Test Case	U_∞ (m/s)	C_{DL}	% Difference from Mean Value
#1: 44 m/s, 0° AOA, Trips	43.93	0.0023	11.5
	44.18	0.0026	0
	44.43	0.0030	15.4
#2: 44 m/s, 0° AOA, No Trips	43.94	0.0021	12.5
	44.19	0.0024	0
	44.44	0.0028	16.7
#3: 44 m/s, 10° AOA, Trips	43.83	0.0032	8.6
	44.08	0.0035	0
	44.33	0.0039	11.4
#4: 44 m/s, 10° AOA, No Trips	43.77	0.0029	9.4
	44.02	0.0032	0
	44.27	0.0036	12.5
#5: 16 m/s, 10° AOA, No Trips	15.73	0.0014	39.1
	15.98	0.0023	0
	16.23	0.0044	91.3

Table 4.3: Effect of the Mean Velocity Fluctuations on the Drag

The results from the table show the striking difference in uncertainty between the high speed test cases and the low speed case. Generally, increasing or decreasing the mean free-stream velocity by 0.25 m/s will increase and decrease the drag coefficients on the order of 0.0004 for the high speed test cases. This corresponds to a 9% to 17% change in the drag coefficient using the original mean velocity; though there was only one instance where the change was greater than 16%. Thus, uncertainty for the high speed cases is probably on the order of 16% or less, suggesting that the results presented can be taken with this level of confidence.

However, for the low speed cases, the change in the drag coefficients was very significant. Setting the mean velocity 0.25 m/s lower produced a coefficient of 0.0014, which was a 39.1% change from the mean data value; while setting the mean velocity 0.25 m/s higher produced a 91.3% change. Thus, the total uncertainty in the data is

difficult to quantify for certain, but it is at least as high as 39% and is probably much higher. Consequentially, the results of the low speed test case probably cannot be taken with very much confidence, though it was thought that the 15.98 m/s free-stream value was a very reasonable estimate to what the mean free-stream value actually was.

4.5 Circulation and Lift Results

4.5.1 Stream-wise Vorticity Profiles

The stream-wise vorticity was calculated and shown in Figures 4.9 – 4.11 for the three test cases with the model at a 10° angle of attack. All profiles were taken one model length downstream of the ellipsoid's trailing edge and the units are s^{-1}. Since the $\frac{V}{U_\infty}$ and $\frac{W}{U_\infty}$ ratios were less than 0.01 and there was no clear vortical structure in the 0° angle of attack test cases, their stream-wise vorticity plots are not shown.

The three vorticity profiles display the same trends as the secondary flow profiles in Figures 4.6 – 4.8, as the vorticity is a by-product of the model's trailing vortices. Like the secondary flow profiles, all of the vorticity profiles are nearly identical in their size, shape, and organization, differing only in their vortical strength and vertical location in the wake survey plane for the two different Reynolds numbers that were tested. For all three plots, the area of vorticity to the right of z = 0 is positive due to the counter-clockwise rotation of the vortex emanating from the model in that location. Likewise, the vorticity to the left of z = 0 is negative due to the clockwise rotation of the other vortex. The strongest region of vorticity in the plots coincides with the location of the centers of the trailing vortices and the vorticity strength greatly diminishes in the free-stream

regions of the wake survey plane. Because of this, it can be said that the rotation of the flow is highest in the center of the vortices and becomes less and less moving out towards the free-stream.

Like what was seen in the secondary flow profiles, the center of the vorticity for test case #5 (Figure 4.11), was positioned 0.05 m above the centers of the vorticity in test cases #3 and #4 (Figures 4.9 and 4.10). Due to the lower free-stream velocity in test case #5 the strength of the vorticity (100 s^{-1}) is also much less than what is seen in test cases #3 and #4 (400 s^{-1}).

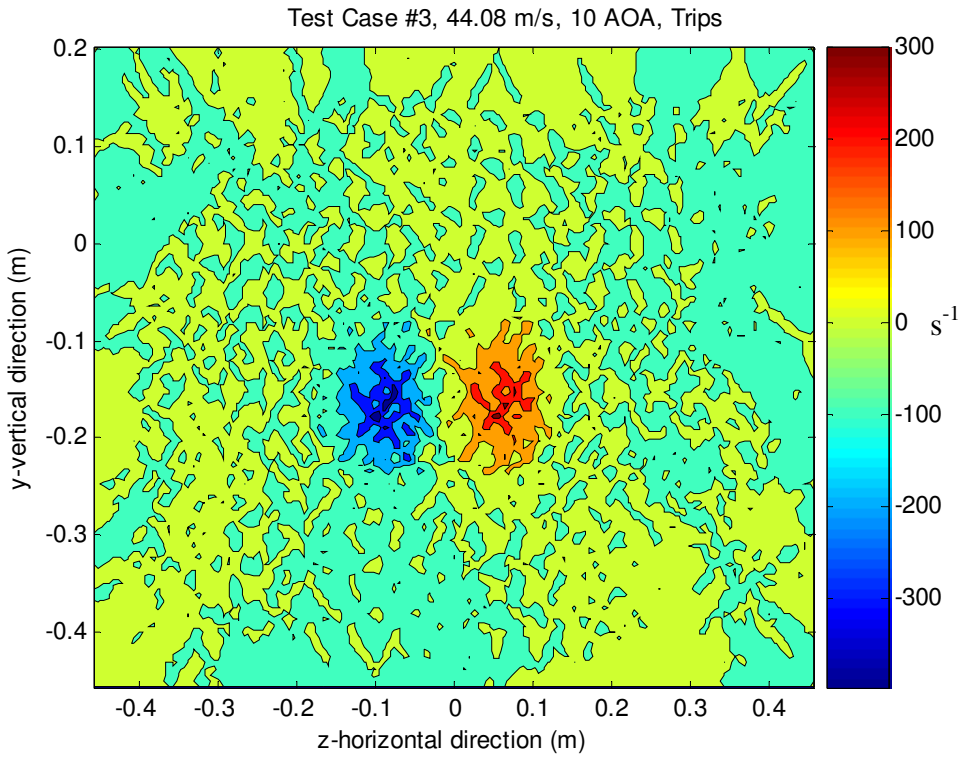

Figure 4.9: Stream-wise Vorticity for Test Case #3 (44.08 m/s free-stream, 10° AOA, trips applied)

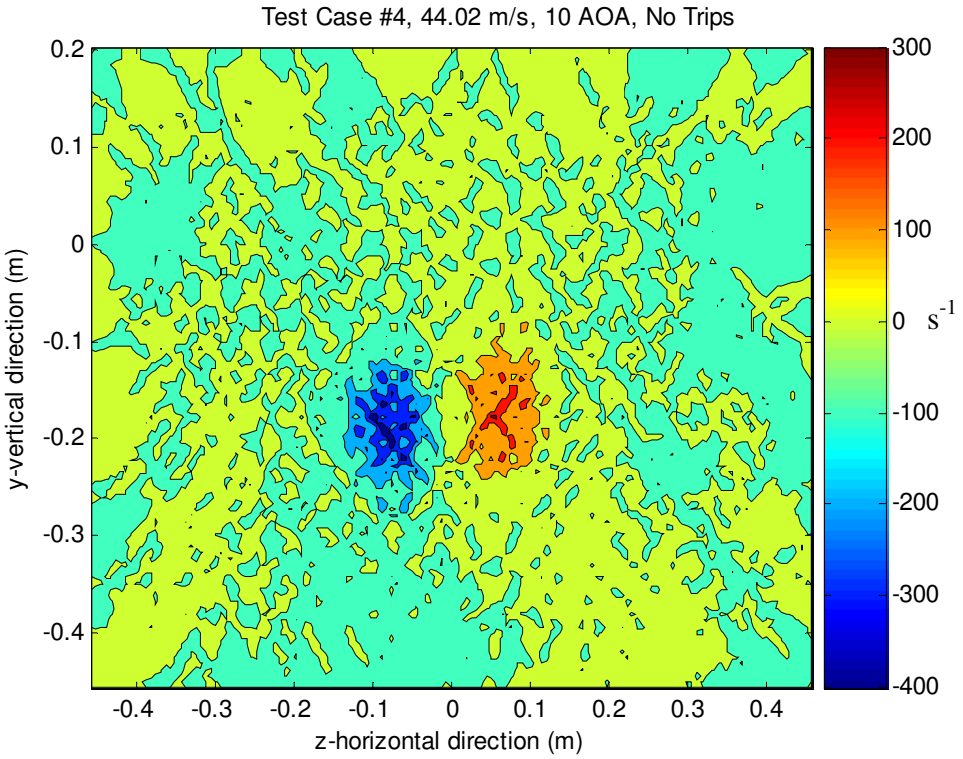

Figure 4.10: Stream-wise Vorticity for Test Case #4 (44.02 m/s free-stream, 10° AOA, no trips)

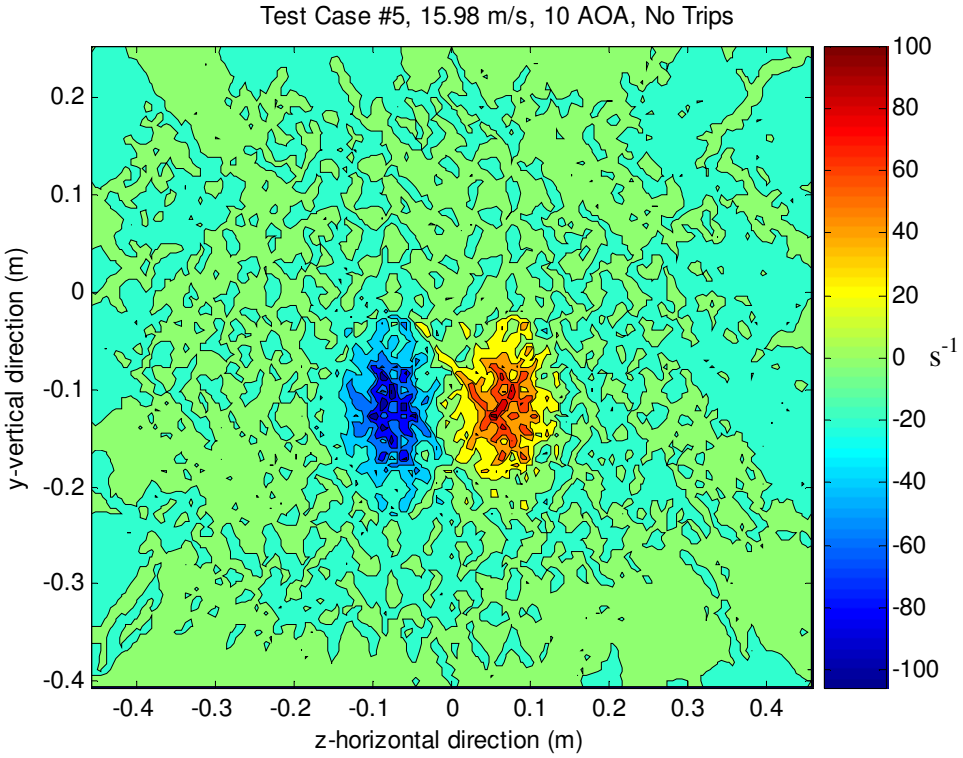

Figure 4.11: Stream-wise Vorticity for Test Case #5 (15.98 m/s free-stream, 10° AOA, no trips)

4.5.2 Circulation

With the vorticity profiles known, Equation 39 could easily be applied to calculate the circulation around each vortex in the wake survey plane for the three test cases at 10° angle of attack. A vertical line at z = 0 divided the integration region for each vortex in the calculation. The circulation results are tabulated in Table 4.4.

Test Case	Circulation of Left Vortex (m^2/s)	Circulation of Right Vortex (m^2/s)	U_∞ (m/s)	Re_L
#3: 44 m/s, 10° AOA, Trips	-2.69	2.80	44.08	4.3×10^6
#4: 44 m/s, 10° AOA, No Trips	-2.61	2.79	44.02	4.3×10^6
#5: 16 m/s, 10° AOA, No Trips	-0.69	0.72	15.98	1.6×10^6

Table 4.4: Summary of Circulation Results

Table 4.4 shows that the circulation for the two high speed cases was nearly the same and significantly stronger than the low speed case. This is due to the higher vorticity in the high speed flow. For all test cases, the magnitude of the circulation of the left vortex is slightly less than that of the right vortex with a 4% to 6% difference. Theory dictates that the circulation of the two vortices should be equal and opposite. This is because Stokes' theorem can be applied to Equation 39 by performing a line integral on a reducible loop that can be drawn around the two vortices in the wake; the net circulation on this line should be zero. Since the circulation of the two vortices is not zero, the percent difference could be indicative of the uncertainty in the calculation.

4.5.3 Lift

The vorticity was also used to calculate the lift on the model with Equation 45 for the three test cases at 10° angle of attack. The entire wake region was used in the integration, so that both vortices were incorporated into the calculation. The results are

tabulated in Table 4.5. Note that three different lift coefficients are presented in the table, C_{LL}, C_{LF}, and C_{LW}. These were normalized with respect to the model's length squared, frontal area, and wetted area, respectively, just like their drag coefficient counterparts that are presented in Equations 46 – 49.

Test Case	Lift (N)	C_L	U_∞ (m/s)	Re_L
#3: 44 m/s, 10° AOA, Trips	21.67	$C_{LL} = 0.0079$ $C_{LF} = 0.2795$ $C_{LW} = 0.0136$	44.08	4.3×10^6
#4: 44 m/s, 10° AOA, No Trips	21.01	$C_{LL} = 0.0077$ $C_{LF} = 0.2699$ $C_{LW} = 0.0132$	44.02	4.3×10^6
#5: 16 m/s, 10° AOA, No Trips	1.84	$C_{LL} = 0.0050$ $C_{LF} = 0.1748$ $C_{LW} = 0.0085$	15.98	1.6×10^6

Table 4.5: Summary of Lift Results

Table 4.5 shows that the two high speed test cases produced lift coefficients that were almost twice as high as the low speed test case. The trips did not seem to have much of an effect on the lift results as the coefficients for the two high speed cases are very close with test case #3 being slightly higher.

4.5.4 Uncertainty in the Circulation and Lift

The uncertainty in the circulation and lift differs considerably from the drag calculations. Unlike the drag, the circulation and lift do not have a noticeable change when the mean value of the free-stream velocity is varied between ± 0.25 m/s. This is due to the fact that the free-stream velocity does not appear in the circulation equation and small changes to the free-stream velocity negligibly affect the result of the lift equation. Thus, the uncertainty in the circulation and lift calculations is probably less

than the drag, which is dominated by human judgment, and comes primarily from the uncertainty in the measurement equipment and the accuracy of the composite trapezoidal numerical integration scheme that was used to the compute both results.

The composite trapezoidal rule is a 2^{nd} order accurate method and for that reason requires a very fine data grid to ensure that uncertainties are kept small. This was the reason behind the interpolation that was done on the original data grid. The grid increment size went from 5.08^2 cm^2 to 0.635^2 cm^2, which is a reduction by a factor of 64. Hence, the error in the composite trapezoidal rule is reduced by a factor of 64^2 or 4096. For this reason, the uncertainty in the integration is probably not very large, but is difficult to quantify for certain.

The uncertainty in the seven-hole probe measurements is reported to be on the order of 1%, so it probably does not contribute too much to the overall uncertainty of the results. However, the difference in the circulation calculated between the two trailing vortices for the three angle of attack test cases is very telling. Since circulation is directly proportional to lift by the Kutta-Joukowski theorem, uncertainties in the circulation calculation are probably the same as those in the lift calculation. Thus, since the circulation of the two vortices are supposed to be equal and opposite but differ for all three angle of attack test cases by around 4% to 6%, uncertainty in the circulation and lift results is probably around 6% or less.

5 Conclusions

A drag study was conducted on a 1.6 m long oblate ellipsoid model having a cross-section of 0.4 m x 0.231 m. The model was constructed from composite materials and suspended by guy wires in the Virginia Tech Stability Wind Tunnel. 2-D wake surveys were taken using a seven-hole probe mounted to a traverse that was one body length downstream of the model. The pressure data from each probe survey was then reduced to determine the velocity profile of the model's wake. The drag could then be calculated by applying the integral momentum theorem to the wake velocity profile. Both the profile and induced drag were calculated and added together to determine the total drag on the model. Additionally, the circulation and lift on the body mounted at a 10° angle of attack was found by integrating the stream-wise vorticity in the wake survey plane.

The experiment was conducted under several different flow conditions and model configurations to determine their effects on the drag measurements. Data were collected with the model in a straight-and-level position (0° angle of attack and yaw) and a 10° angle of attack position (0° yaw angle) with respect to the oncoming flow. For both model positions, data were taken with and without flow trip strips. At the 0° angle of attack position, tests were conducted at 44 m/s. At the 10° angle of attack position, tests were conducted at two different speeds (44 m/s and 16 m/s) to determine the effect of Reynolds number on the drag. These speeds gave length-based Reynolds numbers of 4.3 and 1.6 million respectively.

The results from the drag calculations indicated that mounting the model at a 10° angle of attack increased the length-squared drag coefficient by about 33% to 35% from the straight-and-level cases. This is due to the addition of induced drag that was absent in

the straight-and-level cases and an increase in the profile drag due to the increase in the frontal area of the body that was exposed to the incoming wind.

Adding trip strips to the model appeared to only have a slight effect on the drag results. The length-squared drag coefficient was seen to increase by a small amount perhaps due to an increase in area or roughening up the model surface. However this increase was on the order of 0.0003, when uncertainties on the coefficient for the tests were around ± 0.0004; so the effect of adding the trips may be insignificant. Due to this result and the angle of attack results, test case #3, which was a 10° angle of attack case with trip strips, had the highest length-squared drag coefficient at 0.0035. This was followed by test case #4 at 0.0032, which was also elevated but had no trips. Then came test case #1, which was straight-and-level with trips; it had a drag coefficient of 0.0026. Lastly, test case #2, which was the same as case #1 without trips, had a coefficient of 0.0024.

The effect of decreasing the Reynolds number from 4.3 to 1.6 million in test case #5 of the 10° angle of attack cases was to dramatically decrease the length-squared drag coefficient to 0.0023. However, uncertainties at the lower Reynolds number were so high that this result may be insignificant. Uncertainties for the four high Reynolds number cases were estimated to be around 16%, which seems reasonable. However, at the lower Reynolds number, the uncertainty was at least as high as 39%.

Spatial fluctuations in the free-stream velocity values and human judgment were the main sources of uncertainty in the drag results. To perform the drag calculations, the free-stream had to be made uniform by removing wire wakes and choosing representative mean values for the velocity, pressure, density, and temperature. Spatial fluctuations of

0.2 m/s to 0.3 m/s in the free-stream velocity ensured that there would be an elevated level of uncertainty in the drag results. Because of this, future testing at Reynolds numbers below 2 million may not be advisable using the techniques in this study due to the high uncertainties in the results. However, testing above Reynolds numbers of 4.3 million should further decrease the uncertainty in the drag calculations.

Results from the velocity profiles of the wake showed that a pair of counter-rotating vortices dominated the wake of the three 10° angle of attack test cases. These vortices were absent in the two 0° angle of attack test cases. The reason for this is that the 10° angle of attack test cases created a pressure differential between the upper and lower surfaces of the model, while no differential existed when the model was mounted straight-and-level. It was the pressure differential that produced lift, induced drag, and the counter-rotating vortices on the 10° angle of attack test cases. Since the counter-rotating vortices were absent from the 0° angle of attack cases, no lift or induced drag was produced.

The counter-rotating vortices also produced a downwash effect on the wake. Since the vortices were absent from the 0° angle of attack test cases, their wake remained centered in the center of the tunnel test section. However, the downwash from the vortices caused the center of the wake for the two high speed 10° angle of attack test cases to move downwards by 0.18 m in the 1.6 m that the wake traversed from the stern of the model to the probe tip. The low speed angle of attack test case also had downwash from the vortices, but its wake only moved downwards by 0.13 m over the same 1.6 m distance from the model trailing edge to the wake survey plane. The difference between the angle of downward drift of the wake between the high and low speed test cases may

be attributed to Reynolds number effects on the formation and separation of the counter-rotating vortices on the model.

Using the vorticity produced from the counter-rotating vortices, the circulation around each vortex and the total lift on the model was found. The results indicated that the high speed angle of attack test cases produced stronger circulation and much higher lift coefficients on the model than the lower speed angle of attack test case. The addition of trip strips on the model did not appear to have much of an effect on the circulation or lift produced in the two high speed angle of attack test cases, as their results were nearly identical. Uncertainty in the lift and circulation calculations was estimated to be around 6%, since the difference in the circulation that was calculated between the two counter-rotating vortices in the wake was between 4% and 6% for the three angle of attack test cases.

Overall, much information was obtained from the five test cases. However, time restraints prevented a more detailed drag study. The repeatability of the results was not tested. It also would have been interesting to have results at several different angles of attack, roll, and yaw and different Reynolds numbers to better quantify their effects on the drag.

References

Barlow, J., Rae, W., and Pope, A. *Low Speed Wind Tunnel Testing*. 3rd Ed. Wiley Interscience. 1999. pp. 176-179.

Betz, A. "A Method for the Direct Determination of Profile Drag." *ZFM*, Vol.16, 1925. p. 42.

Brune, G. "Quantitative Low-Speed Wake Surveys." *Journal of Aircraft*, Vol. 31, N2, March 1994. pp. 249-255.

Choi, K. and Simpson, R. "Some Mean Velocity Turbulence and Unsteadiness Characteristics of the VPI & SU Stability Wind Tunnel." *VPI-AOE-161*, Department of Aerospace and Ocean Engineering, Virginia Tech, Blacksburg, VA. 1987.

DeMoss, J. and Simpson, R. "Wind Tunnel Measurements on a NNEMO Model." *VPI-AOE-303*. Department of Aerospace and Ocean Engineering, Virginia Tech, Blacksburg, VA. 2006.

Dress, D. "Drag Measurements on a Modified Prolate Spheroid Using a Magnetic Suspension and Balance System." *Journal of Aircraft*, Vol. 27, N6, June 1990. pp. 523-528.

Eberly, D. "Least Squares Fitting of Data." Magic Software Inc. http://www.magic-software.com. 2001.

Fussell, J. and Simpson, R. "Laminar Boundary Layer Calculations on a Submarine Body, Sail, and Stern Appendages, Using Integral Boundary Layer Equations." *VPI-AOE-274*, Department of Aerospace and Ocean Engineering, Virginia Tech, Blacksburg, VA. 2000. pp. 2-14.

Granlund, K. "On the Stability of Non-Body of Revolution Slender Bodies." PhD Dissertation (in progress), Department of Aerospace and Ocean Engineering, Virginia Tech, Blacksburg, VA. 2007.

Granlund, K. and Simpson, R. "Unsteady Force and Moment Data on a Maneuvering Undersea Vehicle." *AIAA-2004-0729*, 2004. pp. 1-10.

Hoerner, S. *Fluid Dynamic Drag*. Hoerner Fluid Dynamics. 1965. p. 6.16.

Johansen, E., Rediniotis, O., and Jones, G. "The Compressible Calibration of Miniature Multi-Hole Probes." *Journal of Fluid Engineering*, Vol. 123, 2001. pp. 128-138.

Kusunose, K. “Development of a Universal Wake Survey Data Analysis Code.” *AIAA-1997-2294*, 1997. pp. 617-626.

Maskell, E. "Progress Towards a Method for the Measurement of the Components of the Drag of a Wing of Finite Span." *RAE Technical Report 72232*. 1972.

Pisterman, K. “Velocity Gradient and Turbulence Effects on Seven-Hole Probe Velocity Measurements.” MS Thesis, Department of Aerospace and Ocean Engineering, Virginia Tech, Blacksburg, VA. 2004. pp. 6-21, 121-124.

Schetz, J. *Boundary Layer Analysis*. Prentice Hall Inc. 1993. p. 198.

Simpson, R. “Some Experience with the Dynamic-Plunge-Pitch-Roll (DyPPiR) Mount in Unsteady Aerodynamics Research.” *AIAA-2002-0170*, invited paper, 40th AIAA Aerospace Sciences Meeting, Reno, Nevada, January 14 – 17, 2002.

“Stability Wind Tunnel.” Virginia Tech Department of Aerospace and Ocean Engineering. http://www.aoe.vt.edu/research/facilities/stab/. 2007.

Van Dam, C., et al. “Drag Calculations of Wings Using Euler Methods.” *AIAA-1991-0338*, 1991. pp. 2-3.

Whitfield, C. “Steady and Unsteady Force and Moment Data on a DARPA2 Submarine.” MS Thesis, Department of Aerospace and Ocean Engineering, Virginia Tech, Blacksburg, VA. 1999. pp. 20-24.

Wu, J., Hackett, J., and Lilley, D. "A Generalized Wake-Integral Approach for Drag Determination in Three-Dimensional Flows." *AIAA 1979-0279*, 1979. pp. 3-5.

Zsoldos, J. “An Experimental Investigation of Interacting Wing-Tip Vortex Pairs.” MS Thesis, Department of Aerospace and Ocean Engineering, Virginia Tech, Blacksburg, VA. 1992. pp. 10-11.

Vita

Joshua Andrew DeMoss was born in Roanoke, Virginia and grew up in the community of Blue Ridge in Botetourt County. He graduated from both Lord Botetourt High School and the Roanoke Valley Governor's School in June of 2000, having been honored as the class valedictorian at Lord Botetourt. Joshua began his studies towards a B.S. degree in Aerospace Engineering at the Virginia Polytechnic Institute and State University in Blacksburg, Virginia in August of 2000. During his time at Virginia Tech, Joshua served as a co-op student at the NASA Langley Research center for the entire year of 2003 and during the summers of 2002, 2004, and 2005. Joshua graduated Summa Cum Laude in May 2005 and decided to stay at Virginia Tech to pursue his M.S. and Ph.D. degrees in Aerospace Engineering. Joshua was married in July of 2006, and currently resides in Blacksburg with his wife, Andrea, as he completes his education.